Spectroscopic Studies of Tissue Using Near-Infrared Raman Microscopy

Marcus Gustafsson

Master's Thesis
Lund Reports on Atomic Physics, LRAP-207
Lund, January 1997

This thesis was submitted to the
Faculty of Technology at Lund University
in partial fulfilment of the requirements for
the degree of Master of Science.

Abstract

Raman scattering is an inelastic light scattering process resulting from the interaction of light and molecules. This study utilizes Raman microscopy, which combines Raman spectroscopy and microscopy, for microspectroscopic measurements. The instrumentation was based on a Kr^+-laser emitting at 752.5 nm, an optical microscope, a single stage spectrograph and a CCD detector. Spectra of liquid chemicals, laser dyes, pure tissue constituents and various tissues from pig heart were recorded in the region 500–1800 cm^{-1}. The spectra are analysed and observed Raman bands are assigned to specific molecular vibrations. The results show that Raman microspectroscopy is a powerful technique for spectral characterization of tissue and may be interesting for medical diagnosis.

Contents

1 Introduction

1.1 Background and Purpose

Optical spectroscopy provides a possibility to study physical and chemical changes occurring in different tissues, and thereby offering techniques for non-invasive medical diagnostics. In principal, a radiation source is used to perturb a system of atoms and molecules with electromagnetic radiation. By analysing their response, some conclusions might be drawn about the system that was studied. Several techniques for optical spectroscopy are available, e.g. fluorescence, Raman and IR absorption spectroscopy, which are sensitive to the chemical composition and the structure of bio-molecules. Laser-induced fluorescence has been used extensively for clinical applications, allowing disease progression to be monitored *in vivo*. Raman spectroscopy, which is based on inelastic scattering of photons when light interacts with molecules, is not as well established in medicine as fluorescence spectroscopy. On the other hand, Raman spectroscopy has a great potential to provide much more detailed information on the molecular level of tissues and thereby improve the possibility to detect changes which might occur in tissue as a result of a medical disorder. The main difficulties of this technique are the weak signal intensity and the severe disturbance from fluorescence emission. However, in the near-infrared wavelength region of the electromagnetic spectrum, only weak tissue fluorescence is observed and it is possible to acquire Raman spectra with acceptable signal-to-noise ratios.

This work has been conducted at the Department of Physics at Lund Institute of Technology. The medical group at the Division of Atomic Physics has successfully developed laser-based techniques for medical fluorescence diagnostics as well as for malignant tumour therapy [1, 2]. Their experience on Raman spectroscopy for diagnostic purposes is rather limited at the moment. However, a few Raman studies [3–5] have been performed within the medical group. The group is now coordinating a project within the framework of the EC-Biomed-II programme to develop optical methods (e.g. Raman spectroscopy) to identify diseased cardiovascular tissue.

Raman spectroscopy has shown to be an interesting tool for the identification of atherosclerosis [6–11], which is a common vascular disease, cf. Section 1.2. This study presents spectroscopic characterization of tissue by Raman microscopy, concentrating on tissue structures of interest in the diagnosis of atherosclerosis. Raman microscopy combines Raman spectroscopy and optical microscopy, and is a powerful technique for microspectroscopy. The project has focused on the following main subjects:

- Introduction to the theory of Raman scattering and the practise of Raman spectroscopy, especially the technique for Raman microscopy.

- Recording and analysing Raman spectra of pure tissue constituents and tissue samples.

1.2 The Disease Atherosclerosis

Arteriosclerosis is the generic term for vascular disease, causing thickening and inelasticity of the arteries. The most prevalent arterial disorder is *atherosclerosis*, which affects almost every individual to some extent. The major complications of atherosclerosis are ischemic heart disease, myocardial infarction and stroke.

There are wide geographical variations in the incidence of this vascular disorder. Atherosclerosis is responsible for more deaths and serious morbidity than any other disease in the industrialized regions, such as North America, North and Western Europe, and Australia. Nearly 50% of all deaths in the US are attributed to atherosclerosis-related diseases [12]. The death rates are remarkably low in Asia, Africa, and South and Central America.

Atherosclerosis has been the subject for an enormous amount of research and a number of risk factors has been identified. Males are more prone to atherosclerosis than females and the risk increases with age. Other risk factors include:

- Hypertension; An increase in blood pressure is at all ages a major risk factor for atherosclerosis.

- Cigarette smoking; Atherosclerosis is more severe and extensive among cigarette smokers than among non-smooking persons.

- Diabetes; It is well-known that diabetics have a substantially greater risk for developing vascular related diseases.

- High-cholesterol diets and physical inactivity; Diets rich in saturated fatty acids and cholesterol as well as non-regular physical exercise result in an increased incidence of atherosclerosis.

This section is divided into two subsections. The first describes the normal structure of arteries, which is important to be familiar with when further discussing the arterial disease atherosclerosis in the second subsection.

1.2.1 Arteries

Arteries are blood vessels that transport blood from the heart through a system of successively smaller vessels to support the tissues of the body with oxygen-rich blood[a] and nourishment. Depending on the diameter and proportions of different tissue types

[a] There is one exception: the pulmonary arteries transport oxygen-depleted blood to the lungs for oxygenation and removal of access carbon dioxide.

present in the vascular walls, arteries are classified into: (1) elastic arteries, the largest arteries, including the aorta and its major branches; (2) muscular arteries, such as the coronary and renal arteries, distribute blood to individual organs; (3) small arteries or arterioles, which are found just before the capillaries, the smallest blood vessels. The vascular wall of an artery, independent of the vessel size, is composed of three basic concentric layers, see Fig. 1.1. The innermost layer, the *intima*, consists of lining endothelial cells, a fine network of connective tissue, and a dense membrane of elastic fibres (internal elastic lamina). The *media*, or middle coat, is rich in elastic fibres separated by smooth muscle cells. The outer layer (the *adventitia*) is a connective tissue composed of collagen and elastic fibres in which minute blood vessels and nerves are dispersed.

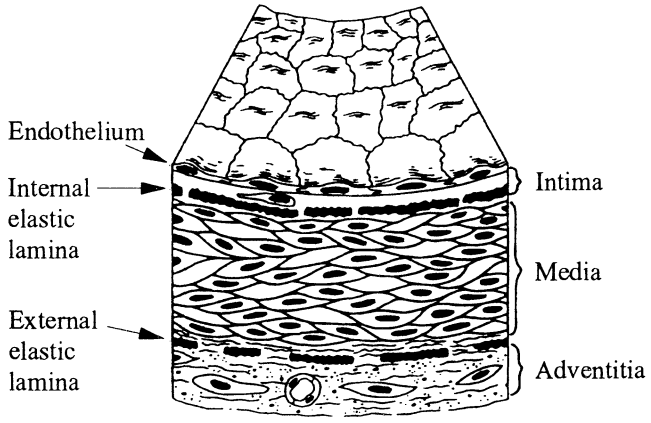

***Fig. 1.1** Schematic drawing of the main components in a muscular artery wall. Modified from [12].*

1.2.2 Atherosclerosis

Atherosclerosis is an arterial disease characterized by thickening of the intima and thereby narrowing the lumen of the arteries, as illustrated in Fig. 1.2. Because the resistance of a blood vessel to fluid flow is proportional to the fourth power of the diameter. Thus, a small change in the lumen size can have a profound flow-limiting effect. The term "atherosclerosis" is used because the lesion has a soft, lipid-rich part (athere meaning "porridge") and a hard (sclerotic) fibrous component. It is primarily the elastic and muscular arteries that are affected by this disorder.

There has not been complete agreement among scientists regarding the initial structural abnormality of atherosclerosis. One hypothesis states that the earliest changes consist of fatty streaks in the intima. The disease develops by forming patches (plaques) in the arterial intima, due to accumulation of lipids, principally cholesterol and its esters, proliferation of smooth muscle cells and formation of fibrous tissue. These changes may extend to the inner part of the media. In advanced lesions, depositions of calcium salts are observed. Calcification causes loss of elasticity in the arteries resulting in rigid vessels that may rupture.

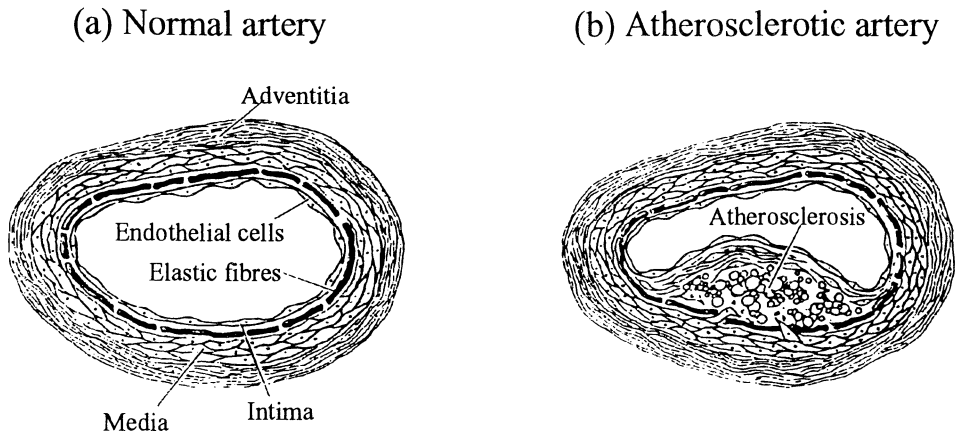

Fig. 1.2 *Schematic cross sections of (a) a normal artery, and (b) an atherosclerotic artery showing the intima thickening which will interfere with the blood flow. Modified from [13].*

2 Theory

The objective of this chapter is to give a brief introduction of Raman spectroscopy, especially the technique of Raman microscopy. The first two sections deal with vibrations of molecules and the origin of Raman scattering. Raman theory is discussed using a classical model based on molecular polarizability, but results of a quantum mechanical approach are also included. Experimental aspects of Raman spectroscopy are discussed in Section 2.3, which ranges from a description of the basic instrumental arrangement to methods for fluorescence discrimination. Section 2.4 describes Raman microscopy, which is a growing field of microprobe spectroscopy and imaging. A discussion about applications of Raman spectroscopy in the field of medicine concludes the chapter.

2.1 Molecular Vibrations

In the quantum mechanical model, electromagnetic radiation consists of photons with energy $E=h\nu_0$, where h is Planck's constant and ν_0 denotes the oscillating frequency of light. Moreover, quantum mechanics states that the energy of a molecule is quantized into discrete energy levels, see Fig. 2.1. The total energy of a molecule is given as the sum of its translational, rotational, vibrational, and electronic energies. Translation occurs when the molecule moves as a whole and the coordinates of its centre of gravity are changed. Translational energy has little effect on molecular spectra. Rotation of a molecule can be regarded as rotation about its principal axes. During vibrations the bond distances and/or angles of the molecule change periodically, but the centre of mass remains constant. Electronic energy corresponds to the arrangement of the electrons. The separation between molecular rotational energy states is in the order of 0.001 eV[a], while vibrational splittings are typically 0.1 eV. The energy levels of electronic states are even further apart and are observed at energies in the order of 1 eV.

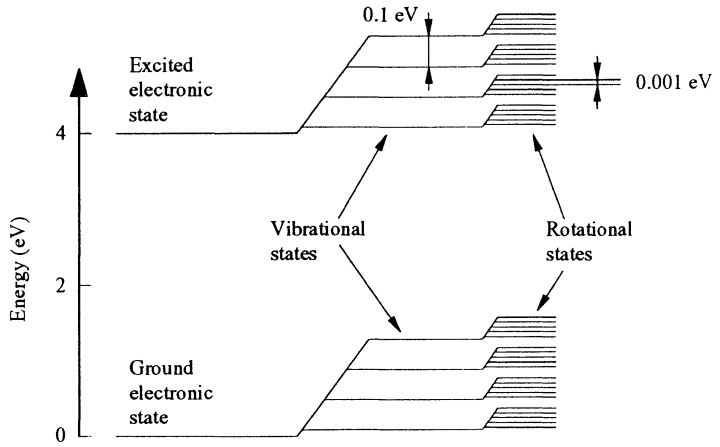

Fig. 2.1 Schematic molecular energy level diagram with rotational, vibrational and electronic states. Modified from [14].

[a] 1 eV ≈ $1.60219 \cdot 10^{-19}$ J

The mass of the atomic nucleus is much heavier and it moves much more slowly than the surrounding electrons. It is assumed that the electrons adjust essentially instantaneously to movements of the nucleus. Thus, the dynamics of a molecule could approximately be described by the motion of its atomic nuclei. The number of degrees of freedom of a particle is equal to the number of coordinates required to specify its position in space. A molecule with N atoms has a total of 3N degrees of freedom corresponding to three independent coordinates for each of the N atoms. If one just considers molecular vibrations, movements referring to rotations and translations must be ignored. The centre of gravity of a molecule requires three coordinates to define its position. This means that it has three degrees of freedom responsible for translation. A molecule requires also three rotational coordinates to specify the molecular orientation about the centre of gravity. Therefore, a molecule has three rotational degrees of freedom. A linear molecule, such as H_2 or CO_2, represents a special case and has only two rotational degrees of freedom. The reason for this is that rotation about the molecular axis is not considered a degree of freedom since no displacements of nuclei are involved. The remaining vibrational degrees of freedom n are

$$n = 3N - 3 - 3 = 3N - 6 \qquad \text{(non-linear molecule)} \qquad (2.1)$$

$$n = 3N - 3 - 2 = 3N - 5 \qquad \text{(linear molecule)} \qquad (2.2)$$

which is identical with the number of normal or fundamental modes of vibration for a molecule. These vibrational modes are defined by:

- All atoms of the molecule move with the same frequency and in phase, but their vibrational amplitudes may be different.
- The vibration does not cause translation or rotation of the molecule as a whole.
- Each normal mode of vibration can be excited independently.

The normal modes of vibration could be classified by type into stretching and bending modes, see Fig. 2.2. The stretching vibration is associated with a motion of atoms causing stretching and shortening of chemical bonds, while bond angles remain unchanged. A bending vibration is a movement of atoms where the angle between bonds changes, but bond lengths are constant. Bendings are further divided into scissoring, wagging, rocking, and twisting. A scissoring mode is an in-plane vibration during which the angle between bonds changes. The wagging vibration is an in-phase, out-of-plane movement. In the rocking vibration, atoms swing back and forth in phase in the symmetry plane of the molecule. Finally, if the plane of atoms is twisted during the vibration, the bending mode is named twisting.

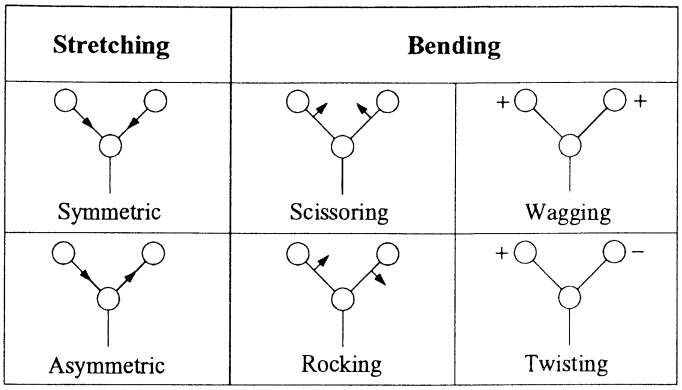

Fig. 2.2 Stretching and bending vibrational modes. The "+" and "–" signs indicate that the atoms move perpendicular to the plane of this page toward and away from the reader, respectively.

Except for the normal modes of vibration that have been described, there are also other types of vibrations:

- Combination bands occur at frequencies ν_c as a combination of frequencies (or multiples thereof) from one or more fundamental vibrations. $\nu_c=a\nu_1\pm b\nu_2\pm...$ where a, b, ... are integers and ν_1, ν_2, ... are frequencies of normal vibrations.

- Overtones can be seen at frequencies ν_o which are multiples of normal vibrational frequencies: $\nu_o=m\nu_1$ with m denoting an integer.

Combinations and overtones are generally observed at much lower intensities compared to normal vibrations. A special case can be observed if the frequency of a combination or an overtone approximately coincides with a normal vibration. Instead of just one strong band from the fundamental, it may happen that two relatively strong bands with almost equal intensities may be observed where only one strong band for the fundamental was expected. These two bands occur on either side of the expected frequency and both contain contributions from the fundamental and the overtone. This effect is called *Fermi resonance*. Molecular anharmonicity causes the appearance of combinations and overtones as well as Fermi resonance bands.

Sometimes a certain normal mode of a molecule is dominated by the vibration of just a few neighbouring atoms forming a functional group. Such a vibration is assigned to that specific group of atoms and the vibrational frequency is known as a *group frequency*. When this functional group is part of another molecule, its group frequency is just slightly affected by the chemical environment. This concept is of enormous practical importance for the identification of functional groups in unknown molecules. For example, proteins, which consist of amino acid chains bound together by peptide linkages, exhibit strong amide vibrations. An amide is the group of atoms forming the peptide bond (–CONH–). Among amide vibrational modes, the amide I and amide III modes are widely studied with Raman spectroscopy. The displacement of the atoms of the peptide bond during these vibrations are shown in Fig. 2.3. The amide I band is mainly due to C=O stretching, but C–N stretching and N–H bending also contribute. The amide III mode is dominated by N–H

bending and C–N stretching. Table 2.1 gives the approximate positions of amide I and amide III vibrations in Raman spectra of proteins with various structures.

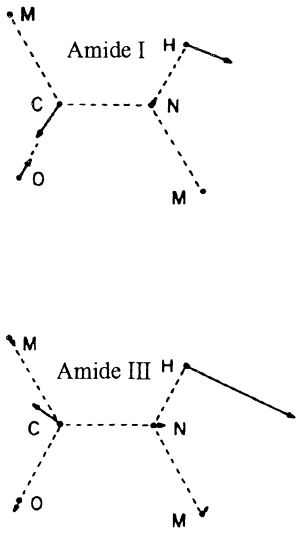

Protein structure	Amide I (cm^{-1})	Amide III (cm^{-1})
α-helix	1645–1660	1265–1300
β–sheet	1665–1680	1230–1240
Unordered	1660–1670	1240–1260

Fig. 2.3 *(left) Illustration of calculated amide I and amide III modes of N-methylacetamide. Modified from [15].*

Table 2.1 *(right) Characteristic group frequencies of amide I and amide III bands in Raman spectra for different protein structures. From [15].*

Frequency is conventionally expressed in Hz, but this unit is inconvenient when studying molecular vibrations because of the high values (~10^{12}–10^{14} Hz). Vibrational spectroscopists have therefore settled on the use of wavenumber, usually expressed in inverse centimetres (cm^{-1}). Wavenumber σ is the reciprocal of wavelength λ, i.e.

$$\sigma = \frac{1}{\lambda} \tag{2.3}$$

Further reading on vibrations of molecules is found in numerous books, for example [R7].

2.2 Raman Scattering

The scattering of light is a fundamental process where electromagnetic radiation interacts with matter. Light scattering results from local fluctuations in the optical properties of a medium. In this process, energy is removed from the incident radiation and reemitted. The scattered electromagnetic radiation might have been subject to a change in direction, frequency and/or phase, as compared to the incident wave. Scattering is essentially instantaneous.

If light is scattered by objects that are small in comparison to the incident wavelength, there are two main scattering effects: Rayleigh and Raman scattering. Rayleigh scattering is an elastic and coherent process, i.e. the frequency of the scattered radiation is equal to that of

the incident light and there is a phase relationship between the incident and scattered radiation. On the other hand, Raman scattering is inelastic and incoherent, i.e. the scattered radiation suffers a frequency shift and a random alteration in phase. The intensity of Raman scattering is roughly one-thousandth that of Rayleigh scattering. In both these processes, the scattered light intensity is proportional to the fourth power of the scattered light frequency. When light interacts with particles of a size much larger than the light wavelength (for instance dust particles), elastic Mie scattering is observed. The probability for Mie scattering is a complicated function of wavelength λ, particle radius r, and other parameters. The cross section increases for shorter wavelengths and is here approximately proportional to λ^{-2}. The frequency dependence of intensity in Rayleigh and Mie scattering is responsible for the fact that the daytime sky looks blue and sunsets are red.

In 1923, A. Smekal predicted the inelastic scattering of light by molecules [16]. A few years later, in 1928, this was observed in the laboratory by the Indian scientist C. V. Raman and his co-worker K. S. Krishnan. During the first experiments Raman and Krishnan used filtered sunlight, which was focused into different kinds of liquids, and they relied on visual observations of the colour changes in the scattered light [17]. Later they used the more powerful mercury lamp and a spectrograph [18, 19]. Almost concurrently the physicists G. Landsberg and L. Mandelstam observed the same phenomena in crystals [20]. The great importance of this light scattering effect was recognized in 1930 when Raman was awarded the Nobel Prize in Physics "for his work on the scattering of light and for the discovery of the effect named after him".

2.2.1 Classical Description of Raman Scattering

Light is an electromagnetic wave of which only the electric component produces Raman scattering. When light interacts with a molecule consisting of electrons and nuclei, the electric field is almost the same throughout the molecule. This could be understood if you compare a molecule of size 1 nm to the wavelength of light, typically 500 nm. Thus, all the electrons in the molecule are accelerated by the same magnitude of force, and they are displaced relative to their average positions resulting in an induced dipole moment.

Suppose that the incident electric field **E** associated with the electromagnetic wave is represented by

$$\mathbf{E} = \mathbf{E}_0 \cos(2\pi\nu_0 t) \tag{2.4}$$

where $E_0=|\mathbf{E}_0|$ is the amplitude of the electric field, ν_0 is the frequency, and t represents the time. For small electric fields, the induced dipole moment **P** is proportional to **E**, i.e.

$$\mathbf{P} = \alpha\mathbf{E} = \alpha\mathbf{E}_0 \cos(2\pi\nu_0 t) \tag{2.5}$$

The coefficient α, the polarizability of the molecule, is a measure of the ease with which the electrons can be distorted under the influence of an applied electric field **E**. The polarizability of a molecule is related to its structure and the nature and direction of its chemical bonds. In general, **P** is not directed in the same direction as **E**. This means that the

polarizability is not a scalar quantity, but a tensor. Using Cartesian components, the equation for **P** could be rewritten as a matrix equation

$$\begin{bmatrix} P_x \\ P_y \\ P_z \end{bmatrix} = \begin{bmatrix} \alpha_{xx} & \alpha_{xy} & \alpha_{xz} \\ \alpha_{yx} & \alpha_{yy} & \alpha_{yz} \\ \alpha_{zx} & \alpha_{zy} & \alpha_{zz} \end{bmatrix} \begin{bmatrix} E_x \\ E_y \\ E_z \end{bmatrix} \tag{2.6}$$

The polarizability tensor α is represented by a symmetric matrix [21, 22], i.e. $\alpha_{ij} = \alpha_{ji}$.

If the irradiated molecule is not just a polarizable sphere but also has vibrating modes, the polarizability will be affected. Assuming these normal modes to be simple harmonic vibrations, the molecule distortion q_k from its equilibrium position for a specific vibrational normal mode k could be described by

$$q_k = q_{0,k} \cos\left(2\pi\nu_{vib,k} t\right) \tag{2.7}$$

where $q_{0,k}$ is the maximal distortion and $\nu_{vib,k}$ is the vibrational frequency of the *k*th vibrational mode. For small vibrating amplitudes, the polarizability could, using a Taylor expansion, be rewritten as (assuming a scalar polarizability α)

$$\alpha = \alpha_0 + \sum_{k=1}^{n} \left(\frac{\partial \alpha}{\partial q_k} \right)_0 q_k + \ldots \tag{2.8}$$

α_0 and $(\partial\alpha/\partial q_k)_0$ represent the polarizability of the molecule and the derivative of the polarizability with respect to the normal coordinate of vibration q_k at the equilibrium position (subscript '0'), respectively. n=3N–6 (or n=3N–5 for linear molecules) gives the number of normal vibrational modes for a molecule consisting of N atoms. Substituting Eq. (2.7) into Eq. (2.8) and then using Eq. (2.5) yields

$$\mathbf{P} = \alpha_0 \mathbf{E}_0 \cos\left(2\pi\nu_0 t\right) + \mathbf{E}_0 \sum_{k=1}^{n} \left(\frac{\partial \alpha}{\partial q_k} \right)_0 q_{0,k} \cos\left(2\pi\nu_0 t\right) \cos\left(2\pi\nu_{vib,k} t\right) \tag{2.9}$$

Then, by making use of the trigonometric identity

$$\cos\theta \cos\varphi = \frac{1}{2}\left[\cos\left(\theta - \varphi\right) + \cos\left(\theta + \varphi\right)\right] \tag{2.10}$$

Eq. (2.9) can be rewritten as

$$\begin{aligned} \mathbf{P} = {} & \alpha_0 \mathbf{E}_0 \cos\left(2\pi\nu_0 t\right) + \\ & + \frac{1}{2} \mathbf{E}_0 \sum_{k=1}^{n} \left(\frac{\partial \alpha}{\partial q_k} \right)_0 q_{0,k} \left[\cos\left(2\pi\left(\nu_0 - \nu_{vib,k}\right)t\right) + \cos\left(2\pi\left(\nu_0 + \nu_{vib,k}\right)t\right)\right] \end{aligned} \tag{2.11}$$

An oscillating electric field **E** that interacts with a molecule will induce an oscillating dipole moment **P**. According to classical electromagnetic theory, an oscillating dipole radiates electromagnetic radiation with the same frequency as the oscillating dipole moment and, therefore, that of the exciting radiation. The molecular vibration, which is much slower than the electric field **E**, causes the induced dipole moment oscillation to be amplitude modulated. This occurs because the molecular polarizability changes when the molecule is stretched or contracted. Thus, the induced dipole moment of a molecule vibrating with frequency $\nu_{vib,k}$ and irradiated at frequency ν_0, will produce elastic Rayleigh scattering at frequency ν_0 but also inelastically scattered Raman components with frequencies $(\nu_0-\nu_{vib,k})$ and $(\nu_0+\nu_{vib,k})$ according to Eq. 2.11. These two inelastic components are called *Stokes Raman scattering* and *anti-Stokes Raman scattering*, respectively. Raman scattering occurs like sidebands on both sides of the Rayleigh line.

2.2.2 Result of a Quantum Mechanical Treatment of Raman Scattering

Classical electromagnetic theory predicts Raman scattering, although a quantum mechanical treatment is needed for a detailed explanation. A complete quantum mechanical analysis will of course not be presented here, but instead some of the interesting results are discussed.

Raman scattering is a process where a photon interacts with a molecule, see Fig. 2.4. The incident photon is not absorbed by the molecule, but the radiation merely perturbs the molecular system inducing a transition from the initial energy state to a so-called *virtual state*. These two states are energetically separated by the energy of the incident photon, $h\nu_0$. The virtual state, unlike ordinary rotational, vibrational and electronic states, is not an actual energy level, rather one which is generally used when discussing Raman theory. Relaxation takes place almost instantaneously to any of the vibrational energy levels of the electronic ground state, indicated by the downward-pointing arrows in Fig. 2.4. The most

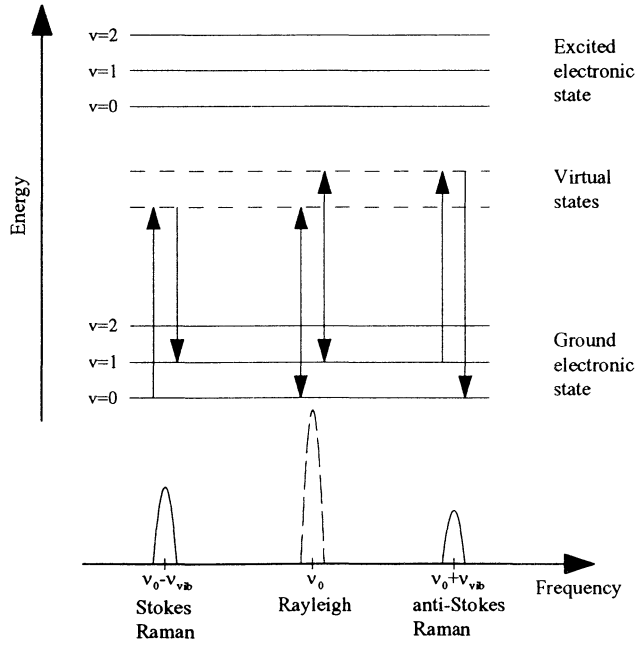

Fig. 2.4 Origin of Raman and Rayleigh scattering.

probable results in elastic Rayleigh scattering, i.e. there is no energy change of the molecule and the scattered photon retains the incident photon energy. Inelastic Raman scattering is observed from two other processes. If the molecule gains energy from the radiation field, the resulting lower-frequency scattered radiation is termed the Stokes Raman component. In this case the change in vibrational quantum number of the molecule is positive, $\Delta v>0$. In the event that the molecule loses energy, the scattered radiation has a higher energy to compensate for this loss and it is referred to as the anti-Stokes Raman component. The change in vibrational quantum number is then negative, $\Delta v<0$.

Raman scattering may also occur for molecular rotational states, but the cross section is even smaller than for vibrational Raman scattering. Rotational Raman scattering is not discussed further in this study.

2.2.3 Raman Activity and Scattering Intensity

Some molecular vibrations have no effect on the molecular polarizability and therefore they do not show any Raman signals. According to Eq. (2.11), the condition for Raman activity associated with the *k*th normal vibration is that (assuming a scalar polarizability α)

$$\left(\frac{\partial\alpha}{\partial q_k}\right)_0 \neq 0 \qquad (2.12)$$

This means that a plot of the polarizability α against the normal coordinate q_k must have a non-zero gradient at the equilibrium position for a Raman active vibration. A theoretical treatment of this can be found in [21].

If one compares the cross sections for different radiation and scattering processes, see Table 2.2, it is obvious that Raman scattering is very weak. These numbers are, of course, not exact values, but they indicate the relative strengths.

Process	Cross section (cm^2)
Resonance absorption	10^{-16}
Fluorescence	10^{-16}
Fluorescence (quenched)	10^{-20}
Rayleigh scattering	10^{-26}
Raman scattering	10^{-29}
Mie scattering	10^{-26}–10^{-8}

Table 2.2 *Cross sections for different radiation and scattering processes. Intense fluorescence occurs at low pressures, but at atmospheric pressure quenching (collisional processes) reduces the intensity. The cross section for Mie scattering varies strongly with the particle size and other parameters. Modified from [14].*

Assuming that an irradiated molecule could be approximated with an oscillating electric dipole, classical electromagnetic theory is applicable. Electromagnetic theory states that the intensity $I_{\text{electric dipole}}$ radiated from an oscillating electric dipole is proportional to the square

of the electric field, which in turn is proportional to the second time derivative of the induced electric dipole moment [23], i.e.

$$I_{\text{electric dipole}} \propto \left(\frac{\partial^2 P}{\partial t^2}\right)^2 \tag{2.13}$$

where P denotes the magnitude of the induced dipole moment **P**. Combining this equation with Eq. (2.11) gives the following intensity relationships for the scattered light

$$I_{\text{Rayleigh}} \propto \nu_0^4 \alpha_0^2 I_0 \tag{2.14}$$

$$I_{\text{Stokes Raman}} \propto \sum_{k=1}^{n} \left(\nu_0 - \nu_{\text{vib},k}\right)^4 \left(\frac{\partial \alpha}{\partial q_k}\right)_0^2 I_0 \tag{2.15}$$

$$I_{\text{anti-Stokes Raman}} \propto \sum_{k=1}^{n} \left(\nu_0 + \nu_{\text{vib},k}\right)^4 \left(\frac{\partial \alpha}{\partial q_k}\right)_0^2 I_0 \tag{2.16}$$

where I_0 is the incident intensity. Eqs. (2.14–16) describe the so-called ν^4 law, i.e. the intensity of the scattered radiation is proportional to the fourth power of the scattered frequency. Since molecular vibrations usually are found at frequencies much less than typical excitation sources, the intensity relationships above demonstrate that the Raman scattered intensities fall rapidly with diminishing excitation frequency ν_0.

The main defiency with the classical theory of Raman scattering is that it predicts an incorrect value for the intensity ratio of the anti-Stokes Raman to Stokes Raman bands. Experiments show that the Stokes components are more intense than the anti-Stokes equivalents. Stokes Raman scattering arises from transitions which finish at a higher vibrational energy level relative to the initial state, whereas anti-Stokes Raman scattering involves a transition from a higher to a lower vibrational energy level. The intensity of Raman scattering is related to the population of the initial state of the molecule. The population of different vibrational energy levels at thermal equilibrium follows the Boltzmann distribution. Thus, at normal room temperature most molecules will occupy the vibrational ground state (v=0) and for higher vibrational energy levels the population decreases exponentially. This results in higher intensity for Stokes Raman scattering compared to anti-Stokes Raman components. The intensity ratio of these two is given by the expression

$$\frac{I_{\text{anti-Stokes Raman}}}{I_{\text{Stokes Raman}}} = \left(\frac{\nu_0 + \nu_{\text{vib}}}{\nu_0 - \nu_{\text{vib}}}\right)^4 \exp\left(-h\nu_{\text{vib}} / kT\right) \tag{2.17}$$

with ν_0 denoting excitation frequency, ν_{vib} molecular vibrational frequency, h Planck's constant, k Boltzmann's constant, and T absolute temperature. As an example, the Raman intensity ratio for an 1000-cm^{-1} molecular vibration at room temperature (300 K) using 752.5-nm excitation equals $I_{\text{anti-Stokes Raman}}/I_{\text{Stokes Raman}} \approx 0.015$. Eq. (2.17) shows also that the

ratio $I_{\text{anti-Stokes Raman}}/I_{\text{Stokes Raman}}$ increases with the temperature because a larger fraction of the molecules will populate excited vibrational states under these circumstances.

2.3 Raman Spectroscopy

Raman spectroscopy is an optical tool for probing vibrational energies in molecules. This technique offers the possibility to identify chemical bonds which vibrate at specific frequencies, i.e. the Raman spectrum provides a molecular vibrational fingerprint. Water and glass are known to be weak Raman scatterers. This is a major advantage when handling samples for Raman spectroscopy. Thus, aqueous materials can be examined, which is important when studying biological systems. The fundamental problem in Raman spectroscopy is the very low intensity of the Raman signal. As a consequence of this, the fluorescence emission from the sample could severely reduce the Raman spectrum quality. During the years, several methods to reduce the effects of this problem have been developed. The interested reader is referred to [15, 21, 22, 24, 25] for a more comprehensive introduction of Raman spectroscopy.

2.3.1 Conventional Instrumentation

In general, the instrumentation designed for Raman spectroscopic studies, is rather simple. One needs intense monochromatic radiation, usually provided by a laser, focused onto the sample to be examined. The Raman scattered light is gathered by collection optics. A monochromator resolves the collected light spectrally and the Raman signal is recorded by a detector. Fig. 2.5 illustrates a typical experimental arrangement for Raman spectroscopy. The instrumental requirements are further discussed below.

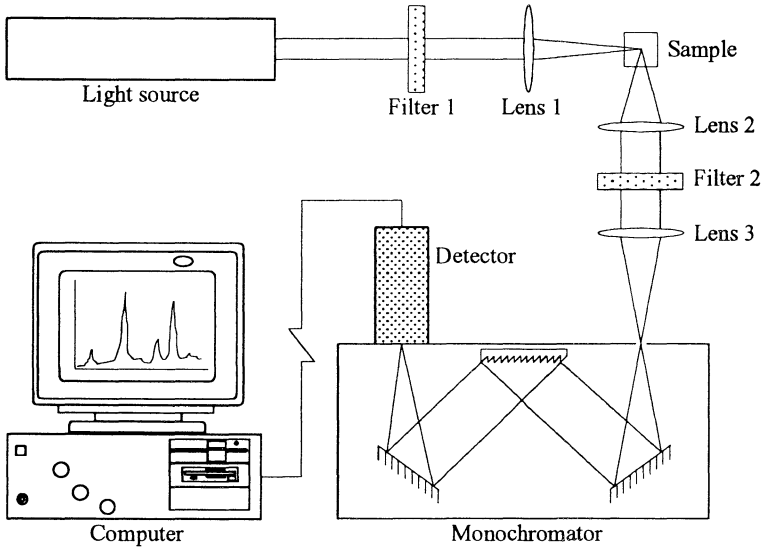

Fig. 2.5 Schematic diagram of a conventional set-up for Raman spectroscopy. Filter 1 is a bandpass filter that removes unwanted emission from the laser, while Filter 2 is a notch filter which suppresses elastic scattered light.

The light source. The laser has proved to be an almost ideal excitation source in Raman spectroscopy. This light source offers a monochromatic light beam of high intensity. Most

Raman experiments use continuous wave (CW) lasers. Pulsed lasers have found their applications in time-resolved Raman spectroscopy (cf. Subsection 2.3.3).

Filters and optics. A laser does not produce perfectly monochromatic radiation, but rather a monochromatic laser beam contamined with weak non-lasing lines which result from spontaneous emissions in the laser cavity. These unwanted emissions are usually called plasma lines (in gas lasers). Of course, plasma lines can be both reflected and Rayleigh scattered by the sample giving rise to spurious bands in the Raman spectrum. This problem is solved by incorporating some kind of filter device (Filter 1 in Fig. 2.5) which eliminates or reduces the intensity of the plasma lines to an acceptable level. A focusing lens (Lens 1 in Fig. 2.5) increases the photon density at the sample resulting in a stronger collected Raman signal. The scattered radiation is gathered by collection optics (Lens 2 and 3 in Fig. 2.5). The first lens (Lens 2 in Fig. 2.5) should have a low f-number[a] which equals a high numerical aperture (N.A.)[b], i.e. light should be collected from the largest possible solid angle. The second lens (Lens 3 in Fig. 2.5) of the collection system is used to focus the light onto the entrance slit of the monochromator, matching its f-number. Before the light enters the monochromator it is needed to discriminate against the strong Rayleigh component in order to minimize stray light within the monochromator. One approach is to incorporate a pre-monochromator, which offers excellent stray light rejection. Developments in optical filter technology have made it possible to construct notch filters of high optical densities, narrow bandwidths and high transmission outside the notch. Inserting such a filter (Filter 2 in Fig. 2.5) in front of the monochromator, increases the throughput and simplifies the set-up compared to the other approach.

The monochromator and detector. The function of the monochromator is to separate spatially the Raman signal on the basis of the frequency. There are two main methods by which the Raman spectrum may be detected. The first is to use a scanning spectrometer with a narrow exit slit and a photomultiplier tube as detector. By turning the grating inside the spectrometer the signal is recorded successively. The second method includes a spectrograph and multichannel detection. The grating of the spectrograph is turned only when changing the spectral region across the detector. CCD (charge-coupled device) detectors are widely applied for this purpose. They offer a relatively high quantum efficiency over a broad wavelength region and extremely low detector noise. This gives the possibility of observing a relatively large spectral bandwidth in real-time.

2.3.2 The Raman Spectrum

The appearance of a Raman spectrum is illustrated in Fig. 2.6 showing the spectrum of carbontetrachloride. A Raman peak corresponds to a vibration of the examined molecule. The horizontal axis is a relative frequency scale and to be more specific it represents the frequency difference between the excitation source and the scattered radiation. The intense Rayleigh signal is located at the zero-point, since this is an elastic process with no

---

[a] The f-number, or f/#, equals f_l/D where f_l is the focal length and D is the diameter of the lens. For example, a lens with 25-mm aperture and a 75-mm focal length has an f-number of 3, which is designated f/3.

[b] N.A. = $n_0 \sin \theta_{max}$ where n_0 represents the refractive index of the immersing medium adjacent to the lens and θ_{max} denotes the maximum half-angle at which light will be accepted.

frequency shift. The Raman frequency shifts are independent of the wavelength of excitation. This means that the location of the Raman peaks are the same whether excitation was carried out with a visible laser or a laser in the near-infrared region. Note that Raman peaks are found on either side of the Rayleigh signal and that the frequency shifts on the two sides are identical. Usually only the Stokes shifted components are studied because they are more intense compared to the anti-Stokes Raman peaks (cf. Eq. 2.17). Characteristic vibrational wavenumbers for Raman peaks of organic compounds are presented in [26, 27].

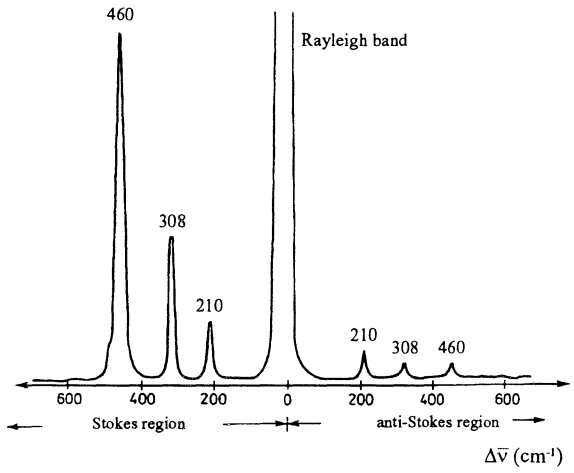

Fig. 2.6 Stokes and anti-Stokes Raman spectrum of carbontetrachloride, CCl_4. Modified from [22].

2.3.3 Fluorescence Reduction

A major drawback of Raman spectroscopy is the fluorescence background that often accompanies the Raman signal. The seriousness of this problem arises from the relatively low efficiency of Raman scattering compared to a typical fluorescence process, cf. Table 2.2. Relative to the Raman signal, the fluorescence background can be enormous, completely obliterating the Raman spectrum. Even if it is possible to observe the Raman signal superimposed on the fluorescence background, the noise contribution of the fluorescence emission degrades the signal-to-noise (S/N) ratio of the Raman spectrum. Several techniques have been developed to minimize the fluorescence interference on the Raman spectrum.

First, a brief introduction to the fluorescence process will be given and then a number of methods to reduce the fluorescence background in Raman spectroscopy are discussed.

An energy level diagram illustrating the main features of molecular fluorescence is given by Fig. 2.7. A molecule that absorbs electromagnetic radiation in the UV or visible region will be excited to any of several vibrational and rotational energy levels of an upper electronic state S_1. Excited states are not stable and therefore the molecule will somehow return to the ground state S_0, i.e. the electronic state of lowest possible energy. The excess rotational and vibrational energy is immediately ($\sim 10^{-12}$ s) lost through radiationless transitions to the lowest vibrational energy level of S_1. These transitions are a consequence of collisions with other molecules and this relaxation process is named *internal conversion*. Deexcitation

from this state will take place in the order of nanoseconds and may occur through several different processes. One possibility for the molecule is to release a photon and then be transferred to any of the rotational-vibrational states of S_0. This emission of radiation is called *fluorescence*. The fluorescence emission is shifted towards longer wavelengths compared to the excitation source due to energy losses during internal conversion in the excited electronic state. The fluorescence spectrum is usually characterized by a broad and rather featureless structure in contrast to a typical Raman spectrum.

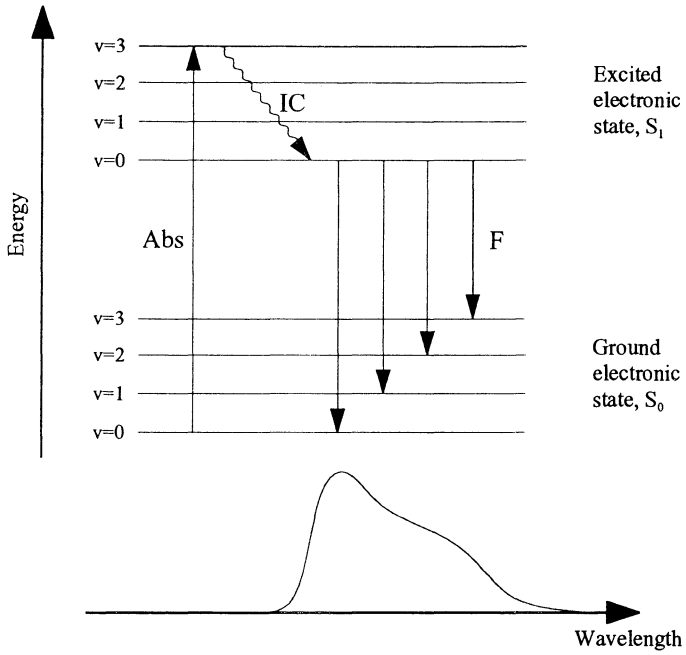

Fig. 2.7 *Schematic energy level diagram of a molecule showing two electronic states, S_0 and S_1, and their vibrational states. Rotational states have been omitted. Absorption of a photon, internal conversion and the following fluorescence emission are illustrated. The abbreviations are: Abs=absorption, IC=internal conversion and F=fluorescence.*

In order to effectively reduce the interference of fluorescence one has to know the properties that differentiate Raman scattering from fluorescence. There are three main differences between these two:

- The Raman spectrum consists of peaks of narrow bandwidth in contrast to the broadband fluorescence emission.
- The lifetime is in the order of 10^{-12} s for Raman scattering, but typically 10^{-9} s in fluorescence.
- Some Raman lines are strongly polarized unlike the unpolarized fluorescence signal.

Several methods, experimental as well as mathematical, have been developed to discriminate against the fluorescence influence on Raman measurements. These techniques either reduce the fluorescence contribution or extract the Raman signal from the measured spectrum. Techniques that utilize the former procedure, i.e. avoid detection of

fluorescence, are attractive since they minimize the noise due to fluorescence emission. A number of possible methods are discussed below.

Near-infrared excitation. Selection of an optimum laser excitation wavelength is effective in suppressing fluorescence according to Fig. 2.8. There are many compounds that absorb in the visible part of the electromagnetic spectrum, giving rise to fluorescence. If one reduces the energy of the excitation photons, i.e. uses a light source with longer wavelength, the energy provided by a photon is not enough to excite the molecule to its first excited band. The excited electronic state will thus not be populated and thereby no fluorescence is produced. Choosing an excitation source within the near-infrared (NIR, ~0.7–2.5 μm) region, a major part of the fluorescence background is eliminated in many cases. Accompanying this advantage are some drawbacks. The cross section for Raman scattering will be reduced due to the ν^4 dependence (see Eqs. 2.15–16) when increasing the excitation wavelength. It is also important that detectors in the near-infrared region have reduced sensitivity and higher noise compared to those in the visible spectral region. The laser wavelength should be extended as far into the near-infrared region of the electromagnetic spectrum as the detector sensitivity permits. This trade-off may change significantly with developments of laser and detector technologies in the future.

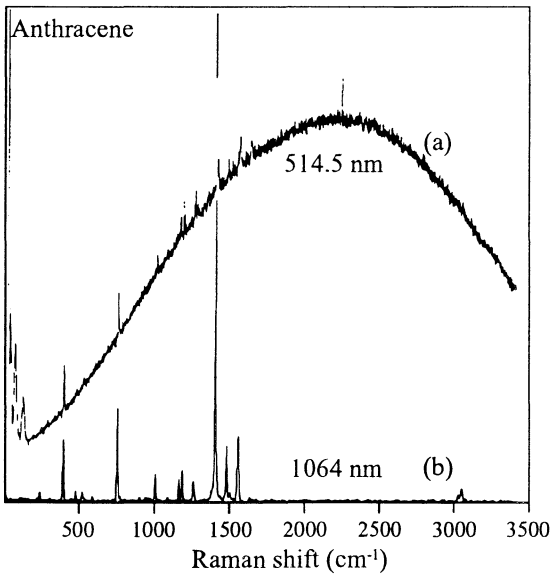

Fig. 2.8 Raman spectrum of anthrancene at (a) 514.5-nm excitation and (b) 1064-nm excitation, respectively. Modified from [28].

Modulation of the excitation wavelength. Tunable lasers have made it possible to illuminate samples with wavelength modulated excitation light. This technique can be used to reject fluorescence [29]. Fluorescence is invariant for small changes of the excitation wavelength, i.e. the fluorescence background remains constant. In contrast, Raman scattered light will follow the modulation of the excitation wavelength. Lock-in detection makes it possible to achieve a derivative Raman spectrum (with respect to wavelength) free from fluorescence. Such a spectrum can easily be integrated to yield the Raman spectrum. Although this technique is effective it requires extra instrumentation for modulation and detection. In addition, lock-in detection precludes multichannel detection resulting in a longer signal accumulation time. A similar technique [30] uses shifted excitation and does

not suffer from these drawbacks. Taking the difference of two Raman spectra, obtained from slightly different excitation wavelengths, gives a signal comparable to the first derivative of the Raman spectrum. Again, the fluorescence background is unchanged but the Raman bands are shifted. A correct Raman spectrum is achieved after integration.

Time-resolved Raman spectroscopy. This technique derives advantage from the disparity in lifetime between Raman scattering ($\sim 10^{-12}$ s) and fluorescence ($\sim 10^{-9}$ s). The idea is to use pulsed laser excitation and time-gated signal detection for S/N improvement of the Raman spectrum. The detector is exposed only for the duration of the Raman signal, but non-active for the relatively long-lived fluorescence emission. Time-resolved Raman spectroscopy has the advantage that you avoid detection of fluorescence photons and thereby reduce the noise contribution. The application of this method has been demonstrated on fluorescent solutions using a picosecond laser and a spectrograph equipped with a streak camera [31]. A disadvantage is that pulsed laser excitation might cause thermal injuries on biological samples because of the high peak intensity of the laser pulses. Note also that short laser pulses will broaden the Raman bands according to the Heisenberg uncertainty relation.

Polarization modulation. Polarization modulation is a differential technique which takes advantage of the Raman lines being highly polarized and the fluorescence being unpolarized [32]. A linearly polarized excitation source is needed for this kind of experiment. Two spectra are measured; one spectrum ($I_{\parallel}$) with the light polarized parallel to the that of the laser and the second spectrum ($I_{\perp}$) with light polarized perpendicular to the first one. For Raman lines that are highly polarized, the intensity will be greater for $I_{\parallel}$. Thus, subtraction ($I_{\parallel}$–$I_{\perp}$) will recover the Raman signal and reject approximately half of the fluorescence background. This Raman spectrum will of course just show peaks with a high degree of polarization.

Polynomial fit. Probably, the simplest and most straightforward method is to fit a polynomial of a degree just enough to describe the broadband fluorescence profile but not the sharp Raman peaks. Subtracting this polynomial from the measured spectrum gives the Raman signal alone. This technique is computationally simple, but there might be negative errors in fit which can cause unintentional subtraction of weak Raman peaks.

FFT. This technique utilizes the same property as the polynomial fit procedure to discriminate the Raman peaks from the fluorescence, but in this procedure fluorescence rejection is achieved in the frequency domain [33]. Broad features, like fluorescence emission, will appear at low spatial frequencies compared to sharp Raman peaks, which will be observed at higher spatial frequencies. A measured spectrum is Fourier transformed by taking the fast Fourier transform (FFT) of the signal. The frequency spectrum is multiplied by a filter function, which attenuates undesirable spatial frequencies, and is then inverse Fourier transformed yielding a spectrum with reduced fluorescence interference. By choosing a suitable filter, the noise contribution could also be decreased.

2.4 Raman Microscopy

Raman microscopy, which combines Raman spectroscopy with microscopy, provides an excellent technique for obtaining information about molecular structure and chemical composition from specimens on a micrometer scale [34]. In 1966, it was suggested that Raman microspectroscopy would be interesting in the analysis of microscopic particles. The first experimental Raman microprobes were developed in the early 1970s [35]. In a typical Raman microscope system, the laser beam passes through the microscope objective which focuses the beam to a diffraction limited spot on the sample. The backscattered photons are gathered by the microscope objective serving as an efficient collection system.

Raman microscopy can be applied for spectroscopic investigations as well as for imaging purposes. In the spectroscopic mode, it is possible to record spectra of small-scale samples or to examine areas of a sample that may be of particular interest with high spatial resolution. Raman microspectroscopy has been applied for the diagnosis of cystnosis (medical disorder characterized by the accumulation of cystine crystals in various tissues) [36], microanalytical characterization of gallstones [37], and others. The other mode, the Raman imaging mode, allows mapping the spatial distribution of molecular species. The laser beam is scanned over the sample, opposed to single point measurements in the spectroscopic mode, which is viewed in the light of discrete wavelength segments of the Raman spectrum forming a multi-spectral image [38]. For example, Raman imaging has been utilized to visulize the cholesterol distribution in a rat eye lens [39].

The depth resolution and image contrast may be enhanced by an confocal instrumental arrangement, i.e. incorporating an aperture into the Raman microscope image plane to reject out-of-focus light, see Fig. 2.9. A smaller pinhole increases resolution and contrast, but the optical throughput is reduced. Detailed assessment of confocal Raman micro-spectroscopy is given in [40], while confocal Raman imaging is demonstrated in [41].

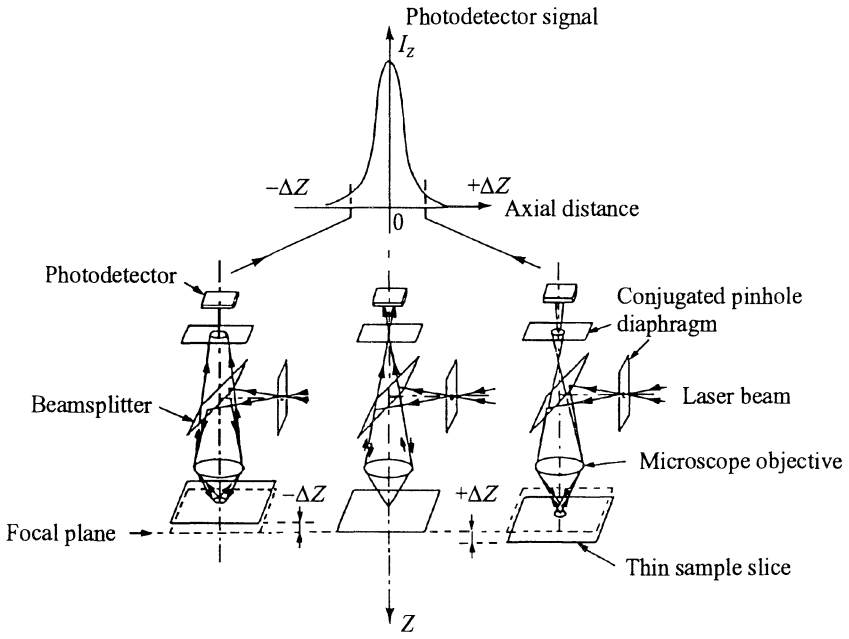

***Fig. 2.9** The effect of sample position on the photodetector signal in a confocal configuration is illustrated. Modified from [34].*

2.5 Medical Applications of Raman Spectroscopy

Raman spectroscopy is a powerful non-invasive technique which has the potential to become a diagnostic tool in medicine. A Raman spectrum provides information on molecular level associated with well-defined and spectrally narrow features. The position of Raman peaks and the relative intensity of different spectral bands can be used to probe the structure of biomolecules in order to distinguish between healthy and diseased biomaterials. However, Raman spectroscopy suffers from the weak signal intensity. Biological media is sensitive to sample heating and the allowed maximum excitation power is therefore limited. In addition, autofluorescence, due to natural chromophores present in tissue, often degrades the quality of Raman spectra. The use of NIR excitation, as a consequence of instrumental improvements, has increased the number of biomedical applications of Raman spectroscopy. Excitation in the NIR region has not only reduced the fluorescence, but gives also the possibility to monitor biological substituents several hundreds of micrometers below the tissue surface.

Several groups have successfully applied Raman spectroscopy for characterization of biomolecules and diagnosis of different diseases. For example, Raman spectra of DNA [15, 22], collagen [6, 42], elastin [6, 42], cholesterol [6, 42], human blood [42, 43], normal aorta [6, 9, 11], atherosclerosis [6–11], human brain tissue [44] are found in the literature. Recently, the developments in diagnostic Raman spectroscopy for precancers and cancers have been reviewed [45]. Excellent spectra from the amino acids tyrosine and tryptophan have been reported [42].

3 Material and Methods

3.1 Instrumentation

The general principles of conventional instrumentation for Raman spectroscopy were discussed in Subsection 2.3.1. Fig. 3.1 shows the experimental arrangement that was used for Raman microscopy. The Raman microscope has been utilized for spectroscopic measurements in this study, no Raman imaging was performed.

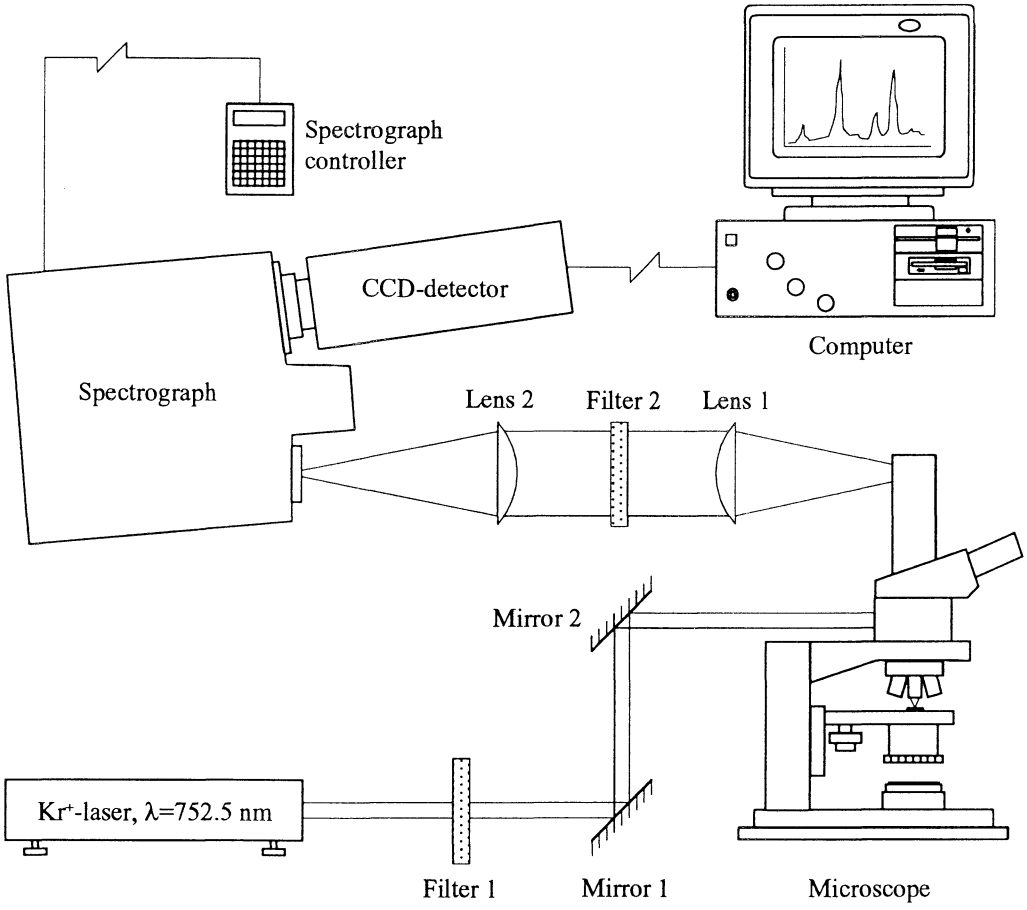

Fig. 3.1 *Schematic diagram of the set-up for Raman microscopy. Filter 1 was a bandpass filter that removed laser plasma lines, while Filter 2 was a notch filter which reduced elastic scattering.*

The light source was a CW Kr^+-laser, which was cooled by water. There are a number of discrete wavelengths available from this laser given in Table 3.1. Changing laser lines was done by choosing the correct laser optics and tuning a prism inside the laser cavity. The 752.5-nm laser line was chosen for excitation with respect to laser output power and fluorescence minimization, cf. Subsection 2.3.3. The laser output passed through an interference filter (Filter 1 in Fig. 3.1; Melles Griot, product number 03FIL055), in order to remove plasma lines. The transmission of this filter was measured to be 67% at 752.5 nm.

Wavelength (nm)	Output powers (W)
793.1–799.3	<0.03
752.5	0.10
676.4	0.15
647.1	0.80
568.2	0.15
530.9	0.20
520.8	0.07
482.5	0.03
476.2	0.05
413.1	0.30
406.7	0.20
356.4	0.12
350.7	0.25

Table 3.1 *Laser lines available from a Kr^+-laser. Output powers for TEM_{00} operation according to power specifications of Coherent Innova 302 [46].*

A pair of gold coated mirrors (Mirror 1 and 2 in Fig. 3.1) directed the laser beam into the microscope (Nikon Labophot-2). Inside the microscope a dichroic mirror was mounted to reflect the laser light through the focusing microscope objective and then onto the specimen to be examined. Two different kinds of objectives were utilized (Nikon, magnification 10×, N.A. 0.45 and S&H, magnification 10×, N.A. 0.25). Approximately, 55 mW of laser light reached the sample of a total of 125 mW laser output power. The backscattered radiation was collected by the same objective, transmitted through the dichroic mirror, and then reflected by a gold mirror (Mirror 3 in Fig. 3.2) inside the microscope tube. The dichroic mirror was chosen to reflect the laser line at 752.5 nm, but to transmit Stokes and anti-Stokes shifted radiation.

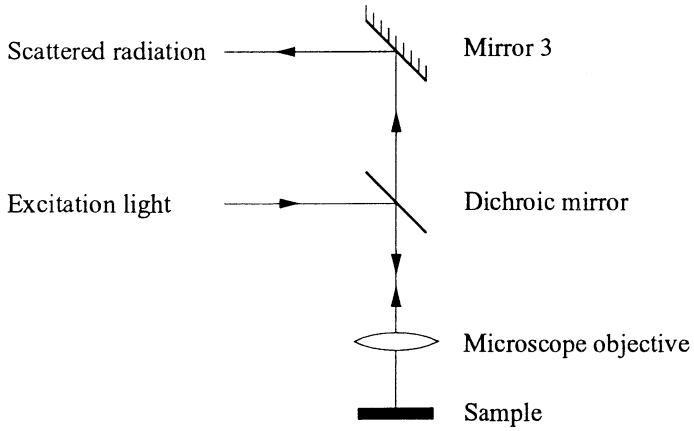

Fig. 3.2 *Schematic of the optical path inside the microscope.*

Elastically scattered light was further suppressed by a holographic notch filter (Filter 2 in Fig. 3.1; Kaiser Optical Systems, part number HNPF-752-1.0) which provided high optical

density (O.D.)[a], >6.0 O.D., at the laser line, and more than 80% throughput outside the notch. The attenuation of this filter was depending on the incident angle, i.e. light passing at different angles experienced a varying transmittance. Thus, a collimated beam was preferred and this was achieved by inserting a ∅25.4 mm f/6.5 plano-convex lens (Lens 1 in Fig. 3.1) in front of the notch filter. A ∅25.4 mm f/2 plano-convex lens (Lens 2 in Fig. 3.1) focused the collected light onto the entrance slit of the spectrograph. This was a single grating spectrograph of Czerny-Turner configuration (Spex 270M, focal length 270 mm, f/4) equipped with two gratings mounted on a turret: a 150 g/mm grating blazed at 500 nm and a 1200 g/mm grating blazed at 750 nm. The dispersion of these two gratings were 24.8 nm/mm and 3.1 nm/mm at the focal plane, respectively. The entrance slit of the spectrograph could be set in the 0–7000 μm range and was adjusted to 50 μm. All moving parts of the spectrograph were remotely controlled by a hand held controller.

Signal detection was performed with a multichannel system (EG&G Princeton Applied Research, OMA-Vision-CCD system) based on a front-illuminated CCD-detector (Thomson CSF THX-31159A). The detector consisted of 512 × 512 elements, of 19 μm × 19 μm each, with a total sensitive area of 9.7 mm × 9.7 mm. Thus, the dispersions 24.8 nm/mm and 3.1 nm/mm corresponded to a spectral coverage of 240 nm and 30 nm, respectively. Each column of pixels was binned (electronically summed before read-out) to create a horizontal array detector of 512 channels. The CCD was cooled by liquid nitrogen to minimize dark current and the temperature of the detector was set to –120°C giving less than 10 photoelectrons/pixel/hour according to specifications.

3.2 Samples

Initially, measurements were performed on nitrobenzene and toluene which are liquid chemicals. Their structure is illustrated in Fig. 3.3. They were chosen because they were known to show relatively strong Raman signals with a minimum of fluorescence background [3–5]. The purpose of these measurements was to get to know the experimental equipment and to optimize the set-up.

Nitrobenzene Toluene

Fig. 3.3 *The molecule structure of nitrobenzene ($C_6H_5NO_2$) and toluene (C_7H_8).*

In order to examine how to recover the Raman signal from spectra of highly fluorescent compounds, laser dyes were studied. Powder of rhodamine 6G (Lambda Physik) and rhodamine 640 (Exciton) were chosen to be examined and their chemical structure is

---

[a] $O.D. = {}^{10}\log\left(\frac{1}{T}\right)$, where T is the optical transmission.

illustrated in Fig. 3.4. When used as an active medium in a dye laser, rhodamine 6G is tunable from 560 nm to 650 nm, while rhodamine 640 is tunable from 620 nm to 700 nm.

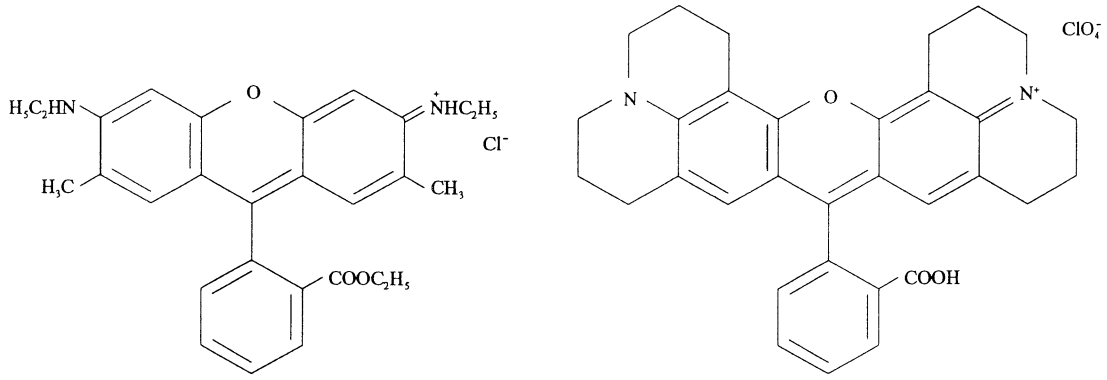

Rhodamine 6G

Rhodamine 640

Fig. 3.4 *The molecule structure of rhodamine 6G ($C_{28}H_{31}N_2O_3Cl$) and rhodamine 640 ($C_{32}H_{31}N_2O_7Cl$).*

The third group of samples were pure tissue constituents, such as cholesterol ($C_{27}H_{46}O$; Sigma Chemical Co., product number C-8667) and NADH ($C_{21}H_{27}N_7O_{14}P_2Na_2$; Sigma Chemical Co., product number N-6005). Cholesterol is known to be accumulated in atherosclerotic plaques. Thus, powder of cholesterol would be of interest to study. The NADH (reduced form of nicotineamide adenine dinucleotide, NAD^+) sample was powder of β-NADH. The ratio of NADH to NAD^+ is different for malignant cells relative to normal tissue.

Unfortunately, there were no human specimens available at the time for measurements and therefore tissue samples from pig heart were examined instead. Samples of aorta, heart tissue and adipose tissue attached to the outer of the heart muscle were chosen. All tissue samples were stored at 8°C after sacrifice and they were examined within 48 hours. The life of a normal pig is rather short, which is the reason why pigs usually do not show any signs of atherosclerosis. Nevertheless, spectra of hydroxyapatite ($Ca_5(OH)(PO_4)_3$; Fluka, product number 55496), which is a calcium salt found in the calcification of advanced atherosclerotic plaques, were recorded.

3.3 Data Analysis

Raman spectra were measured in the 500–1800 cm^{-1} wavenumber region above the excitation wavelength (Stokes Raman spectrum). Both the 150-g/mm and the 1200-g/mm gratings were utilized. Because of the limited spectral coverage of the 1200-g/mm grating, four successively recorded subspectra were put together to obtain a spectrum of the whole wavenumber region. Wavelength calibration was performed with atomic emission lines from a neon discharge lamp. The neon lamp was put in front of the microscope objective and a minimum of four atomic lines were used to calibrate each of the subspectra. The pixel positions of the atomic lines at the CCD detector were fit to a first degree polynomial to give a wavelength scale and then the Raman shifts were calculated relative to the 752.5-nm laser line. All recorded spectra were background subtracted to correct for

an offset in the detector electronics and dark current counts in the CCD chip. The spectra were also calibrated for the wavelength dependent response of the instrumentation using a xenon lamp. Calibrated emission data of the lamp from the manufacturer was divided by a recorded spectrum of the xenon lamp to give the function for instrumental correction.

As discussed in the theory chapter, there are several techniques to overcome the fluorescence problem. The excitation line was chosen in the NIR region to minimize the effects from fluorescence emission. This is often not sufficient, depending on the actual sample there might still be fluorescence interference. In this study, the Raman signal to background ratio was improved further by subtracting the fluorescence background using the polynomial fit procedure as described in Subsection 2.3.3.

4 Results

4.1 Liquid Chemicals

Measurements were initially performed with the 10×, 0.45-N.A. microscope objective. Fig. 4.1 shows the Raman spectra of nitrobenzene and toluene with the 150-g/mm grating. These spectra should be compared with those in Fig. 4.2 where only the grating is changed

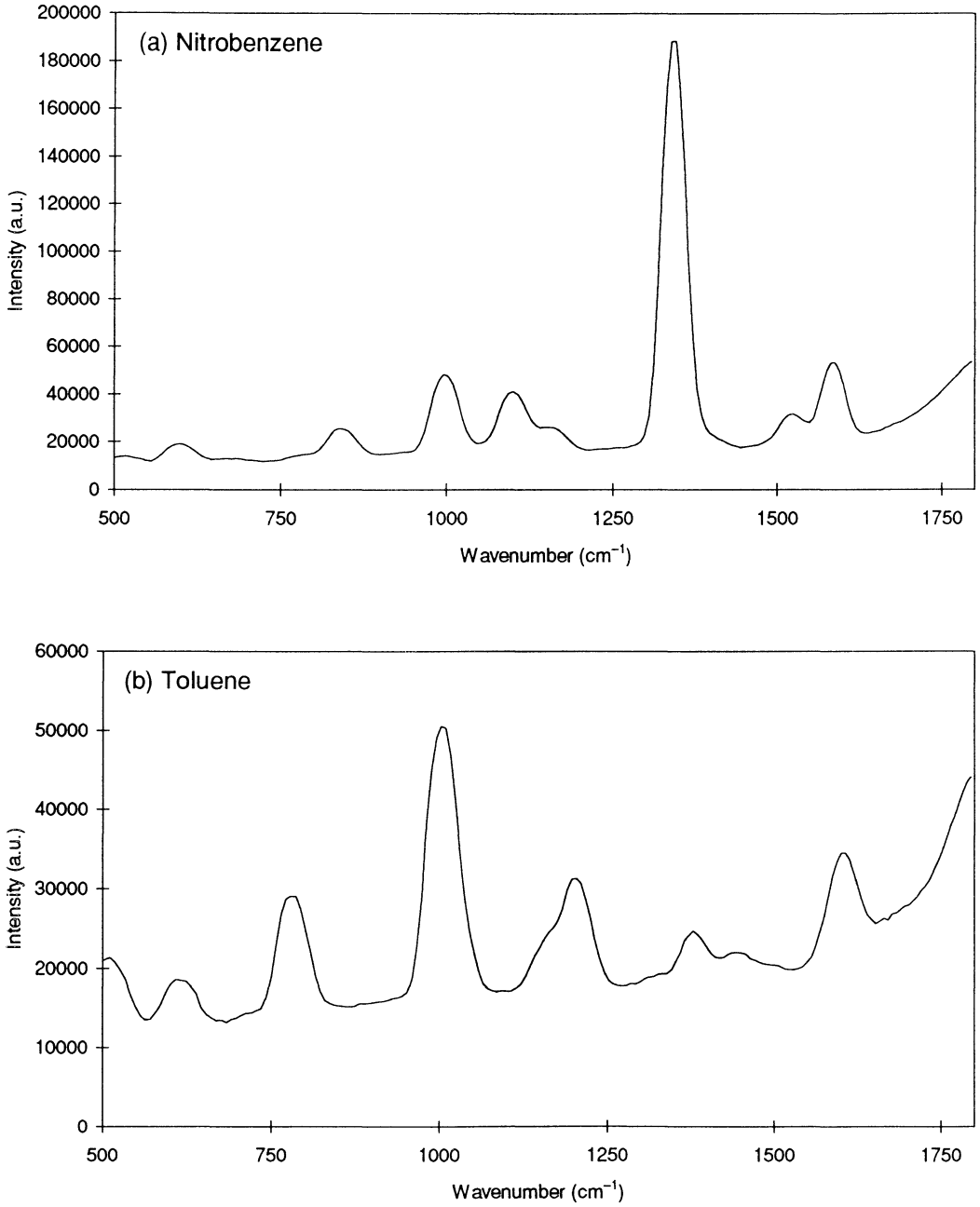

Fig. 4.1 Raman spectra of (a) nitrobenzene and (b) toluene with 150-g/mm grating, 55 mW of excitation power, and 10 s integration time.

to the 1200-g/mm grating. It is obvious that the high-resolution grating was required to reveal the feature of the Raman signal. Thus, the 1200-g/mm grating was utilized for all Raman recordings to come. Fig. 4.3 illustrates Raman spectra of nitrobenzene with various collection times. During the early measurements to optimize the instrumentation, a weak background signal was observed. This broadband emission is not seen in Figs. 4.1–3 because of the intense Raman signal, but the background was clearly observable when spectra were recorded without any sample. The conclusion, after a careful investigation, was that the excitation light gave rise to fluorescence emission from the microscope objective optics. By changing microscope objectives to the 10×, 0.25-N.A. objective, this problem was reduced.

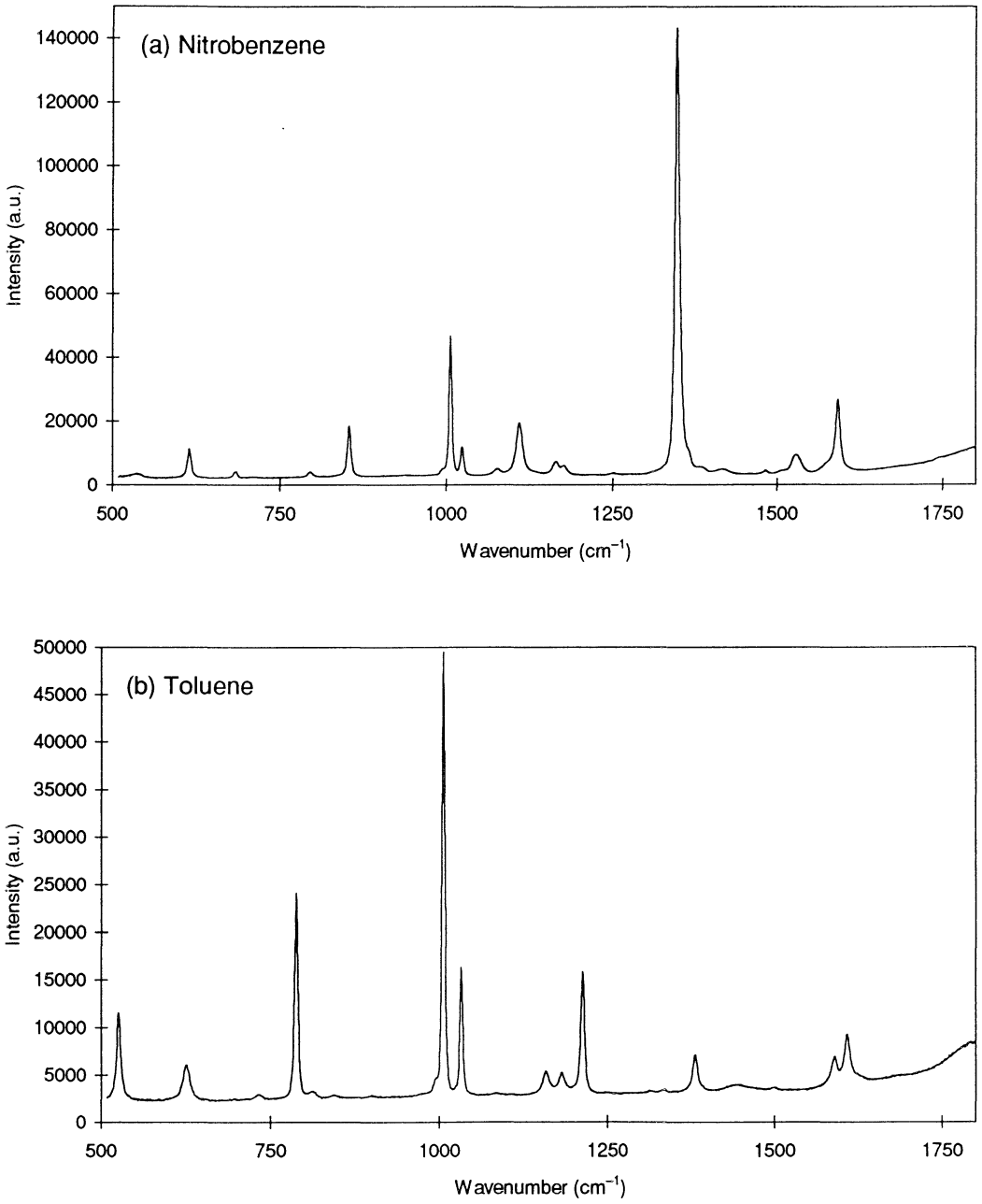

Fig. 4.2 Raman spectra of (a) nitrobenzene and (b) toluene with 1200-g/mm grating, 55 mW of excitation power, and 10 s integration time.

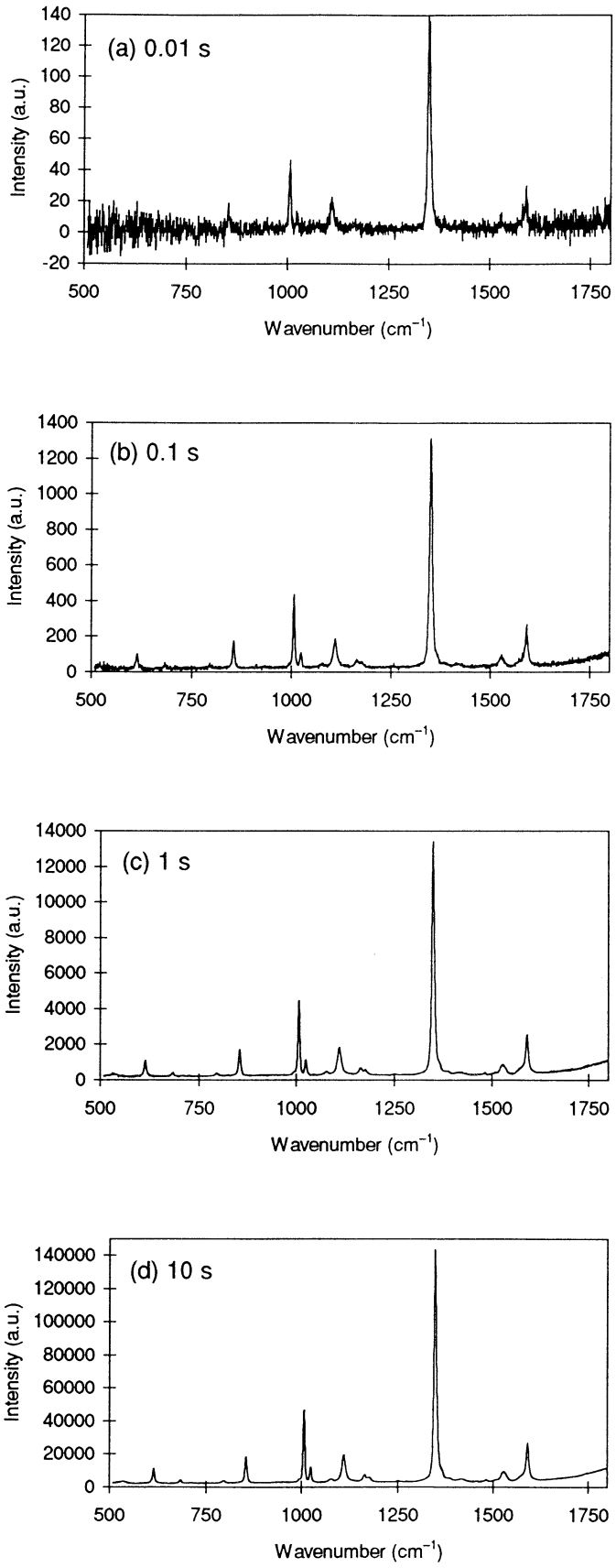

Fig. 4.3 Raman spectra of nitrobenzene with 1200-g/mm grating, 55 mW of excitation power, and integration times (a) 0.01 s, (b) 0.1 s, (c) 1 s, and (d) 10 s.

Not only the fluorescence background was suppressed by applying this objective, but there was also an increase in the signal intensity as shown in Fig. 4.4. The wavenumbers of observed Raman peaks for nitrobenzene and toluene are listed in Table 4.1 together with tabulated wavenumbers.

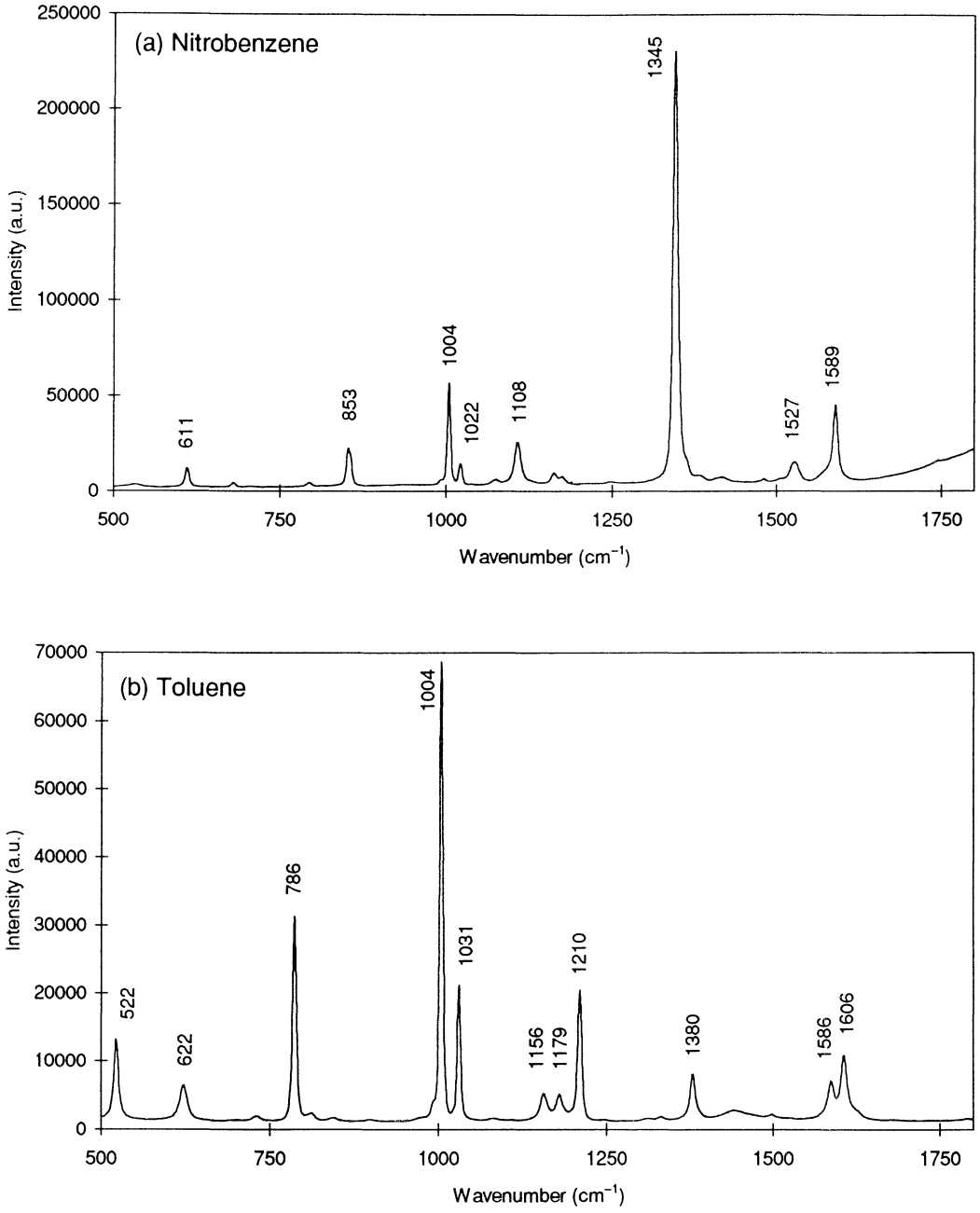

Fig. 4.4 *Raman spectra of (a) nitrobenzene and (b) toluene with 1200-g/mm grating, 55 mW of excitation power, and 10 s integration time.*

(a) Nitrobenzene

Observed Raman shift (cm^{-1})	Tabulated Raman shift[a] (cm^{-1})
611	610
853	850
1004	1001
1022	1020
1108	1106
1345	1345
1527	1523
1589	1588

(b) Toluene

Observed Raman shift (cm^{-1})	Tabulated Raman shift[a] (cm^{-1})
522	521
622	
786	788
1004	1001
1031	1028
1156	
1179	
1210	1210
1380	1380
1586	
1605	1606

Table 4.1 *Observed and tabulated Raman shifts for (a) nitrobenzene and (b) toluene.*

4.2 Laser Dyes

Measurements on laser dyes, such as rhodamine 6G and rhodamine 640, were performed in order to study highly fluorescent samples. An excitation power of 55 mW caused thermal damage to the dyes, therefore the excitation power was reduced to approximately 10 mW and the laser beam was also defocused to further decrease the intensity at the sample.

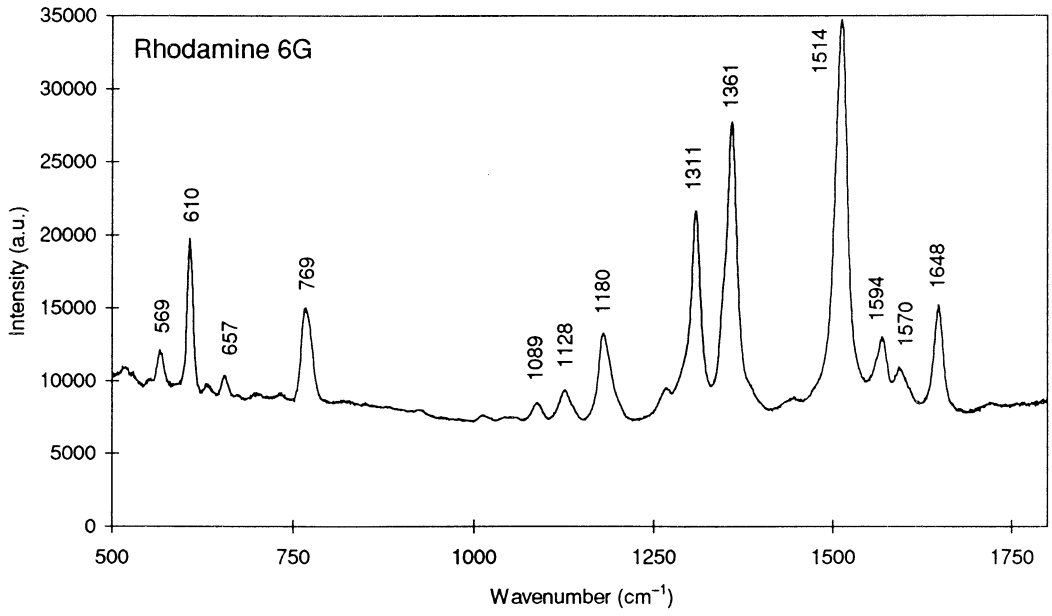

Fig. 4.5 *Fluorescence and Raman emission from rhodamine 6G. The spectrum was recorded with 1200-g/mm grating, 10 mW of excitation power, and 1 s integration time.*

[a] From [27].

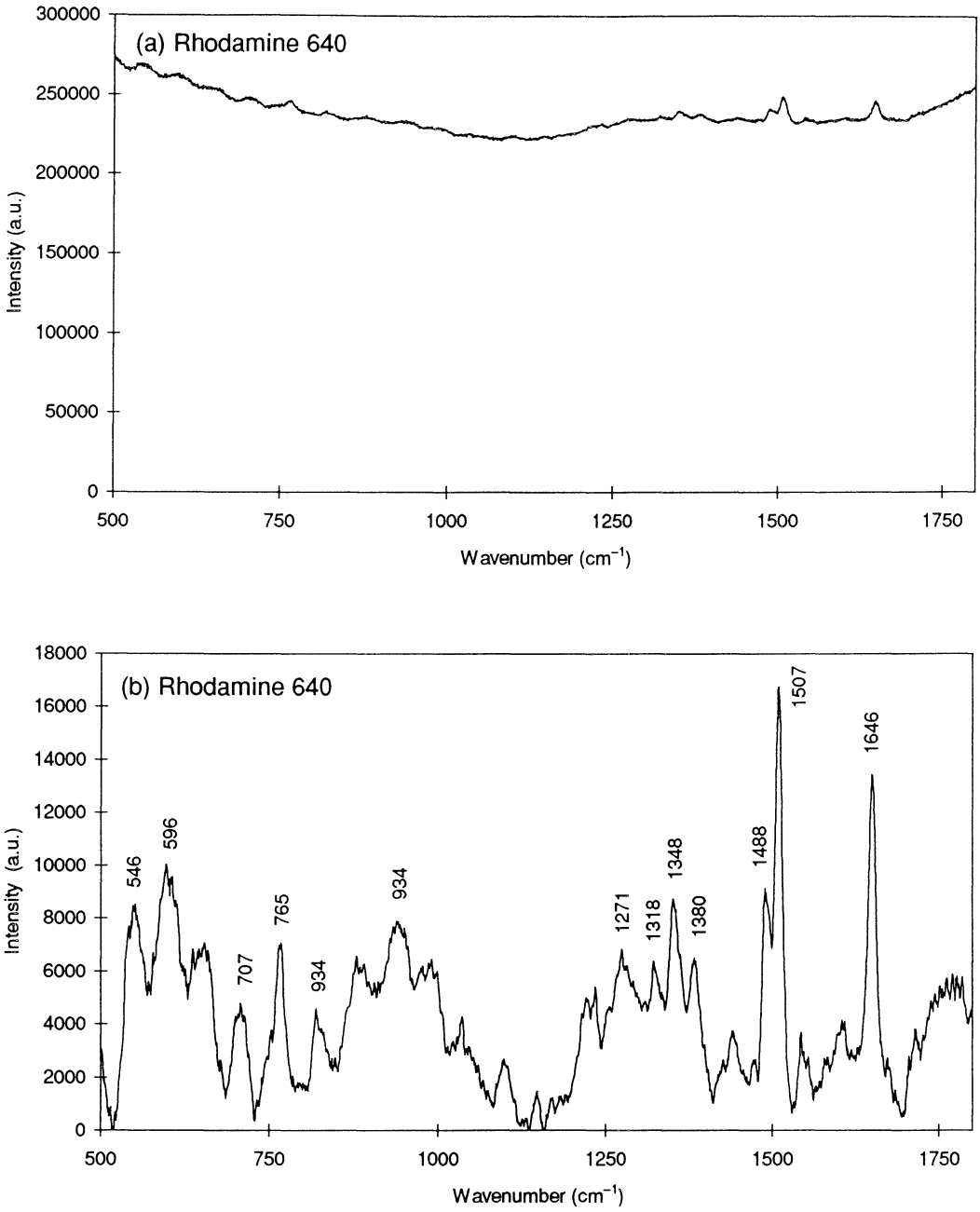

Fig. 4.6 *(a) Fluorescence and Raman emission from rhodamine 640. The fluorescence background has been subtracted and data has also been average filtered in (b), illustrating the Raman spectra of rhodamine 640. Spectra were recorded with 1200-g/mm grating, 10 mW of excitation power, and 5 s integration time.*

4.3 Pure Tissue Constituents

Raman spectra of cholesterol and NADH are shown in Fig. 4.7. The observed Raman peaks of cholesterol are listed in Table 4.2.

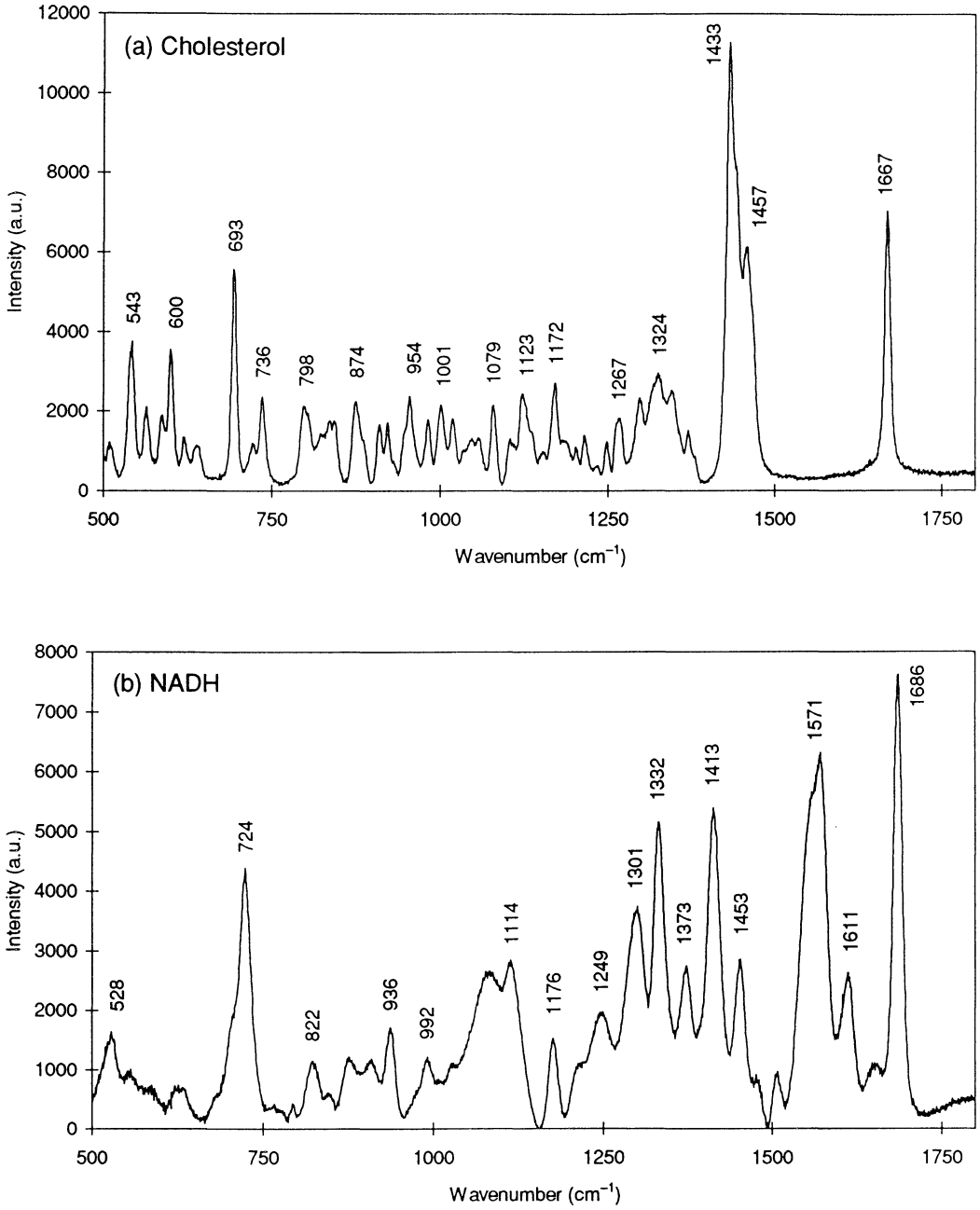

Fig. 4.7 Raman spectra of (a) cholesterol and (b) NADH with 1200-g/mm grating, 55 mW of excitation power, and 30 s integration time. The fluorescence background has been subtracted.

Cholesterol

Observed Raman shift (cm^{-1})	Raman shift[a] (cm^{-1})	Raman shift[b] (cm^{-1})	Raman shift[c] (cm^{-1})
543	550	545	
564	570	570	
600	600	603	
620	620	627–640	
693	693	700	
736	732	745	739
798	798	803	
	812	815	812
	830	846	842
874		885	876
		925	918
954	950	960	957
981	975		
	992	990	
1001	1010		
1018	1020	1020	
	1050	1050	1055
1079	1068		
	1090	1088	1086
	1116		
1123	1125	1132	
	1156		
1172	1162	1178	
1215	1200	1194	
	1235	1220	
1248	1252	1258	
1267	1280	1272	
1297	1300	1300	1296
1324	1328	1326	1327
1345	1358		
1370	1364	1390	
1433	1444	1448	1437
1667	1668	1673	1666
			1727

Table 4.2 *Observed and tabulated Raman shifts for cholesterol.*

[a] Raman bands for anhydrous cholesterol [47].
[b] Raman bands for cholesterol monohydrate [47].
[c] Raman bands for cholesterol [42].

4.4 Tissue Samples

Tissue samples from pig heart were examined, but also powder of hydroxyapatite. Spectra of aorta (intimal side), heart tissue and adipose tissue are illustrated in Fig. 4.8, while the Raman spectrum of hydroxyapaptite is shown in Fig. 4.9. The major vibrational modes identified in aorta and adipose tissue are listed in Table 4.3.

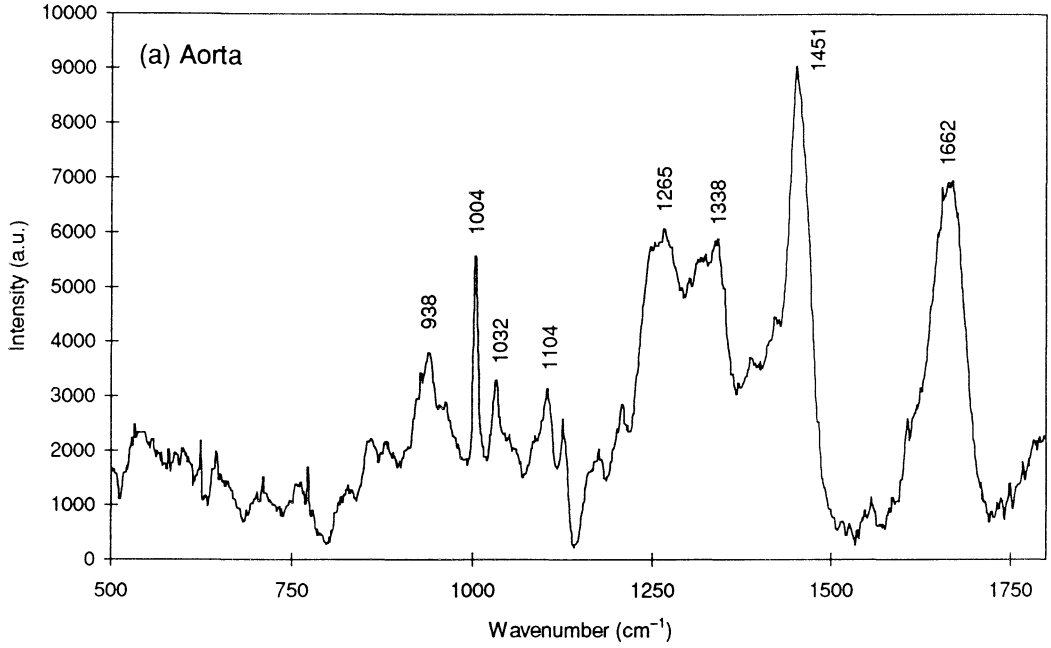

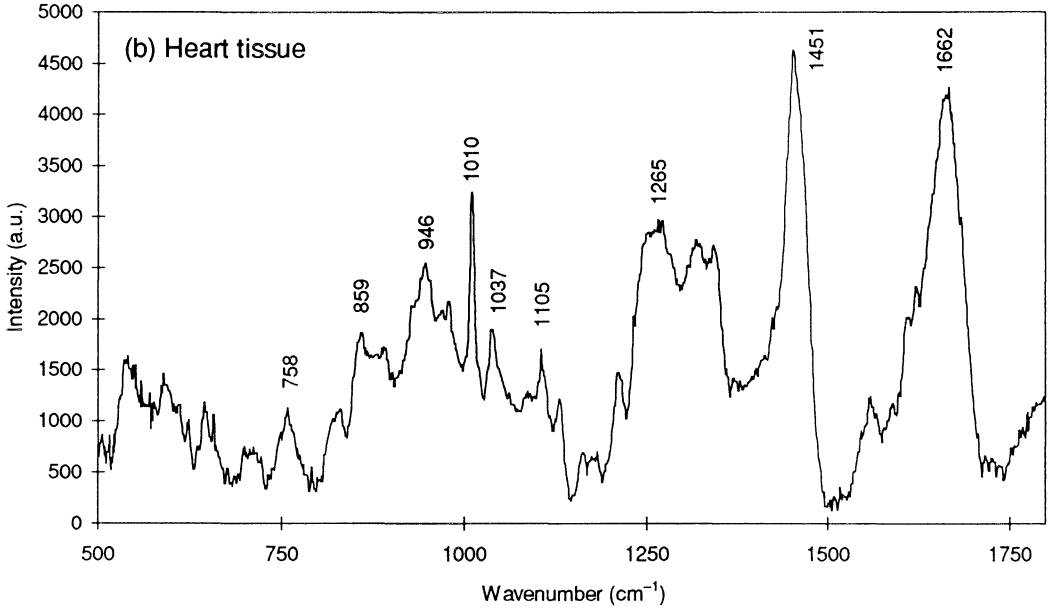

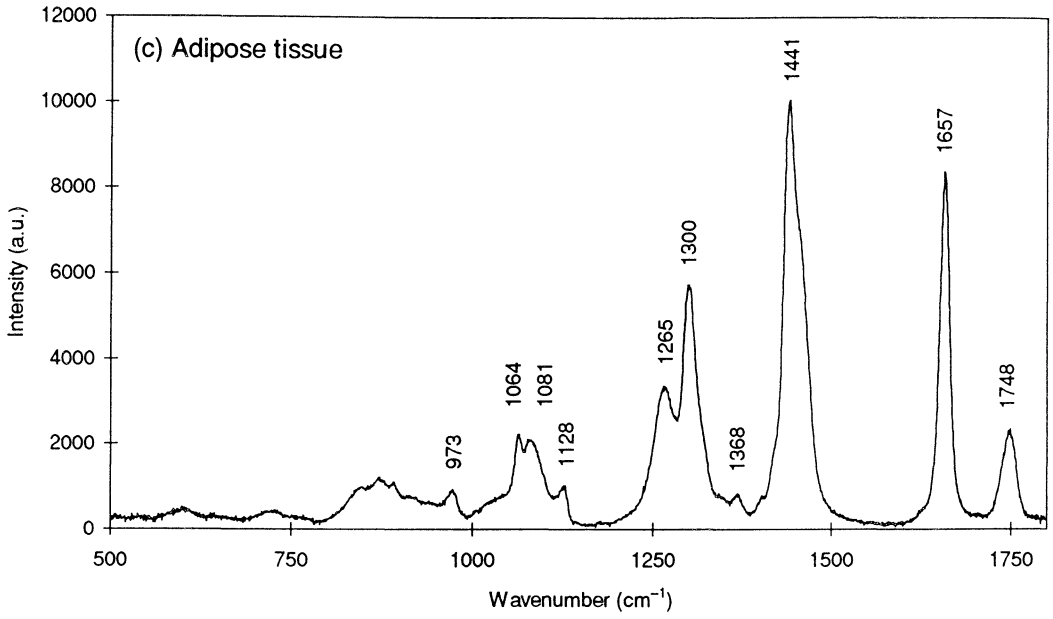

Fig. 4.8 Raman spectra of tissues from pig heart: (a) aorta, (b) heart tissue and (c) adipose tissue. Spectra were recorded with 1200-g/mm grating, 55 mW of excitation power. In (a, b), the integration time was 300 s and data has been median filtered to remove peaks due to cosmic ray interference, while 30 s acquisition time was used in (c). The fluorescence background has been subtracted in all spectra.

(a) Aorta

Observed Raman shift (cm^{-1})	Raman shift[a] (cm^{-1})
938	
1004	1004
1032	
1104	
1265	1252
1338	1335
1451	1453
1662	1658

(b) Adipose tissue

Observed Raman shift (cm^{-1})	Raman shift[b] (cm^{-1})	Raman shift[c] (cm^{-1})
	864	
973		
1064		
1081	1080	1080
1128		
1265	1267	1265
1300	1301	1300
1368		
1441	1440	1438
1657	1655	1654
1748	1746	1746

***Table 4.3** Observed Raman bands in (a) aorta and (b) adipose tissue.*

[a] Normal human aorta irradiated from the intimal side [11].
[b] Normal human aorta irradiated from the advential side (primarily adipose tissue) [11].
[c] Fat from adult golden Syrian hamster [48].

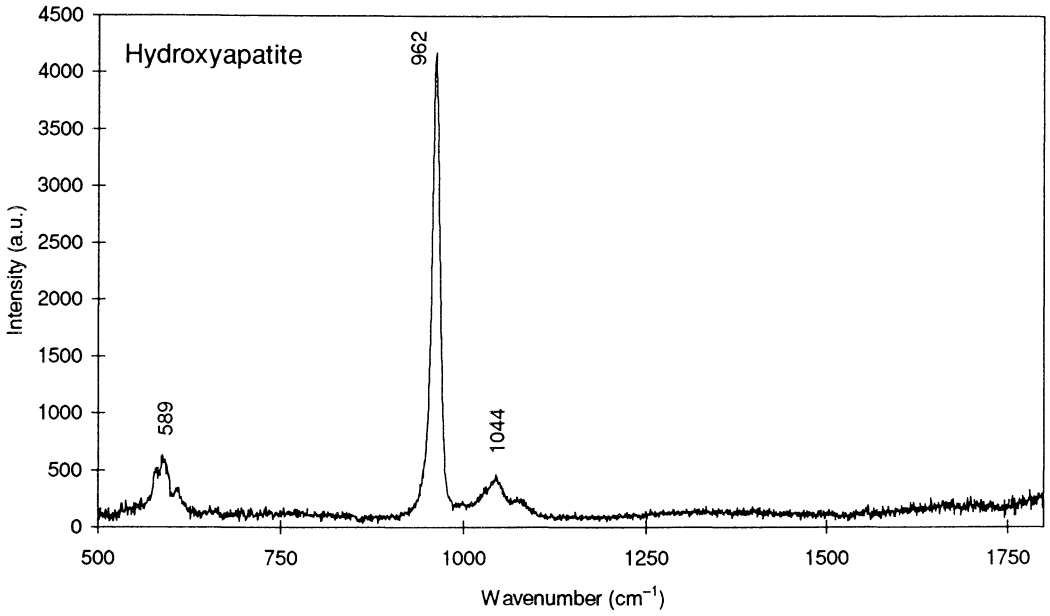

Fig. 4.9 *Raman spectra of hydroxyapatite with 1200-g/mm grating, 55 mW of excitation power, and 30 s integration time. The fluorescence background has been subtracted.*

5 Discussion and Conclusions

5.1 Discussion

The aim of the initial measurements on liquid chemicals was to give an introduction to the Raman instrumentation as mentioned before. From Figs. 4.1–2 it is obvious that the 150-g/mm grating of the spectrograph was not capable of resolving all the Raman bands that were observed with the 1200-g/mm grating. Fig. 4.3 illustrates the spectra of nitrobenzene for different integration times and the main vibrational bands are clearly distinguishable for an acquisition time as short as 10 ms. Measurements on toluene showed the same behaviour, demonstrating the relatively large Raman cross section of the chosen liquid chemicals. After the change of microscope objectives, the detected Raman intensity increased as seen in Fig. 4.4. Not as evident in the figure, is that the new objective also caused less fluorescence emission, which later proved to be of great importance when collecting Raman spectra of tissue samples. Raman spectra of nitrobenzene and toluene show a number of narrow peaks in the spectral region 500–1800 cm^{-1}. The nitrobenzene spectrum is dominated by a very strong vibrational band at 1345 cm^{-1}, which is assigned NO_2 symmetric stretching. The Raman spectrum of toluene contains an intense peak at 1004 cm^{-1} (ring breathing), that was also found in nitrobenzene spectrum, and strong vibrational bands at 786 cm^{-1}, 1031 cm^{-1} and 1210 cm^{-1}. In Table 4.1, the wavenumbers of observed Raman bands of nitrobenzene and toluene are compared with tabulated wavenumbers. The correspondence is good, but not perfect. Wavelength calibration was performed with a neon lamp which was placed in front of the microscope objective. Better results may have been achieved if a Raman active sample with well-defined peaks had been utilized for calibration instead. This method has the advantage that the optical path is identical with the one during later spectral recordings, while using a discharge lamp for calibration, the actual position of the lamp is critical. The chemical indene (C_9H_8) has several accurately measured Raman bands in the 500–1600 cm^{-1} region [49–51] and is becoming a standard for wavelength calibration in Raman spectroscopy.

The interference from fluorescence emission caused no problems at all when studying nitrobenzene and toluene with 752.5-nm excitation. However, the situation changed when Raman spectra of laser dyes were collected. In the spectrum of rhodamine 6G, see Fig. 4.5, there is a broad fluorescence background, but the Raman bands are clearly observable. The acquired signal from rhodamine 640 shown in Fig. 4.6 (a) looked much worse and it is difficult to observe any reproducible Raman signal. After subtraction of a polynomial, that was fitted to the broadband fluorescence, the Raman spectrum is recovered as illustrated in Fig. 4.6 (b). This simple technique for fluorescence rejection has the advantage that no sophisticated instrumentation is required (cf. time-resolved Raman spectroscopy). Note that the spectral resolution was reduced during the measurements on laser dyes because the laser beam was defocused.

Cholesterol and NADH are large molecules and are thereby the origin of many vibrational modes (not all of which are Raman active of course). This is clearly illustrated in their Raman spectra as shown in Fig. 4.7. The cholesterol spectrum contains intense peaks at

693 cm^{-1} (sterol ring stretch), 1433 cm^{-1} (CH_2 bending) with a shoulder band at 1457 cm^{-1}, and 1667 cm^{-1} (C=C stretch). The peak due to sterol ring stretch has been proposed to serve as a marker for the detection of cholesterol accumulation in atherosclerotic lesions [6]. In the NADH spectrum, strong Raman bands are observed at 724 cm^{-1}, 1332 cm^{-1}, 1413 cm^{-1}, 1571 cm^{-1} and 1686 cm^{-1}.

Three different tissues from normal pig heart were studied: aorta, heart tissue and adipose tissue and their spectra are illustrated in Fig. 4.8. The samples of aorta and heart tissue showed weak Raman bands and therefore long acquisition times were necessary, while the Raman peaks of adipose tissue were more intense. The aorta sample was irradiated from the intimal side, which show a different spectrum compared to the advential side [11]. The aorta and heart tissue spectra are dominated by vibrational modes attributed to protein vibrations. The 1662-cm^{-1} peak is assigned amide I vibration of the polypeptide chain, the band observed at 1451 cm^{-1} is due to C–H bending of proteins and an amide III mode is found at 1265 cm^{-1}. Both these samples also show a sharp peak located at 1004 cm^{-1} and 1010 cm^{-1} (phenyl ring breathing), respectively, which probably indicates the presence of the amino acid phenylalanine. It is possible that the 1010-cm^{-1} peak found in heart tissue is due instead to another amino acid, tryptophan, but no more tryptophan bands are observed. The spectra of adipose tissue contains a C–H bending mode (1441 cm^{-1}), but no phenyl ring breathing is observed. The C–H bending mode is shifted to a lower wavenumber, which is characteristic of lipids. Moreover, the Raman bands at 1265 cm^{-1} and 1300 cm^{-1} indicate C–H bending and C–C stretching modes of fatty acids, respectively. The sharp peak at 1657 cm^{-1} of adipose tissue is not an amide I vibration, but is assigned C=C stretching in unsaturated fatty acid chains. This vibrational band is found at a slightly different wavenumber and has a smaller bandwidth compared to an amide I vibration. Adipose tissue showed also a C=O stretching band located at 1748 cm^{-1}, which was not found in the other pig tissues. There were no visual signs of damage to the pig tissues that the intense laser radiation might have caused. However, damage can not be excluded without pathological examination after the spectral recording and future work should investigate this matter more carefully.

The Raman spectrum of hydroxyapatite powder in Fig. 4.9 is dominated by the very strong phosphate stretching band at 962 cm^{-1}. This prominent peak would be an excellent marker for the identification of calcified atherosclerotic plaque and its strength would most likely allow real-time detection.

The acquisition time to collect tissue spectra was comparatively long, but it should be possible to reduce the time for spectral recording [5]. Significant advances have been made in basic spectroscopic instrumentation. There are compact spectrographs with much higher throughput compared to the one that was used in this study. Improvements in detector technology have extended the performance and resulted in CCD detectors with increased sensitivity in the NIR. It is believed that Raman measurements will be of great interest for medical diagnostics in the future.

5.2 Conclusions

The primarily purpose of this work was to record Raman spectra of various tissues, concentrating on cardiovascular tissues, using NIR Raman microscopy. Initial measurements on liquid chemicals and laser dyes illustrated the performance of the instrumentation, and baseline subtraction for fluorescence rejection in Raman spectra was also demonstrated. Spectral characterization of aorta and heart tissue showed mainly vibrational bands due to proteins, while the spectrum of adipose tissue was dominated by Raman peaks assigned to lipids. Diagnosis of the arterial disease atherosclerosis seems to be an interesting application of Raman spectroscopy. The band due to sterol ring stretch observed at 693 cm^{-1} in cholesterol and the 962-cm^{-1} vibration (phosphate stretching) of hydroxyapatite are possible markers for this medical disorder.

Acknowledgements

I would like to express my sincere gratitude to my supervisor, Stefan Andersson-Engels, for his guidance during my time at the medical group. I shared a laboratory with Jonas Johansson and really appreciated the support and good advice from him. I am also grateful for the use of his computer. Anders Åkesson is greatly acknowledged for sharing his newly-acquired experience on Raman spectroscopy. Whenever you face a problem with your laser equipment (I really did...), I recommend you to talk to competent persons like Anders Persson and Åke Bergqvist. Claes af Klinteberg was always willing to give a helping hand in situations when needed. I received valuable information about the microscope from Ingrid Rokahr and Andrea Nord helped me to write correct English. Finally, I would like to thank Professor Sune Svanberg who introduced me to the fascinating world of atomic and molecular spectroscopy during interesting and inspiring lectures.

References

1. S. Andersson-Engels, "Laser-Induced Fluorescence for Medical Diagnostics", Ph.D. Thesis, *Lund Reports on Atomic Physics*, **LRAP-108** (Lund Institute of Technology, Sweden, 1989).

2. J. Johansson, "Fluorescence Spectroscopy for Medical and Environmental Diagnostics", Ph.D. Thesis, *Lund Reports on Atomic Physics*, **LRAP-148** (Lund Institute of Technology, Sweden, 1993).

3. U. Gustafsson, "Near-Infrared Raman Spectroscopy Using a Diode Laser and CCD Detector for Tissue Diagnostics", Diploma Work, *Lund Reports on Atomic Physics*, **LRAP-138** (Lund Institute of Technology, Sweden, 1993).

4. J. Bood and H. Carlsson, "Raman and Infrared Absorption Spectroscopy for Tissue Diagnostics", Diploma Work, *Lund Reports on Atomic Physics*, **LRAP-168** (Lund Institute of Technology, Sweden, 1995).

5. A. Åkesson, "Near-Infrared Raman Spectroscopy for Tissue Characterisation: Adoption of the Set-up for Medical Use", Diploma Work, *Lund Reports on Atomic Physics*, **LRAP-198** (Lund Institute of Technology, Sweden, 1996).

6. R. Manoharan, J. J. Baraga, M. S. Feld and R. P. Rava, "Quantitative Histochemical Analysis of Human Artery Using Raman Spectroscopy", *Journal of Photochemistry and Photobiology B: Biology*, **16**, 211–233 (1992).

7. R. H. Clarke, E. B. Hanlon, J. M. Isner and H. Brody, "Laser Raman Spectroscopy of Calcified Atherosclerotic Lesions in Cardiovascular Tissue", *Applied Optics*, **26**, 3175–3177 (1987).

8. R. H. Clarke, Q. Wang and J. M. Isner, "Laser Raman Spectroscopy of Atherosclerotic Lesions in Human Coronary Artery Segments", *Applied Optics*, **27**, 4799–4800 (1988).

9. J. J. Baraga, M. S. Feld and R. P. Rava, "Rapid Near-Infrared Raman Spectroscopy of Human Tissue with a Spectrograph and CCD Detector", *Applied Spectroscopy*, **46**, 187–190 (1992).

10. D. D. Klug, D. L. Singleton and V. M. Walley, "Laser Raman Spectrum of Calcified Human Aorta", *Lasers in Surgery and Medicine*, **12**, 13–17 (1992).

11. J. J. Baraga, M. S. Feld and R. P. Rava, "*In Situ* Optical Histochemistry of Human Artery Using Near Infrared Fourier Transform Raman Spectroscopy", *Proceedings of the National Academy of Sciences of the USA*, **89**, 3473–3477 (1992).

12. S. L. Robbins, *Pathologic Basis of Disease*, 5th ed. (W. B. Saunders Company, Philadelphia, 1994).

13. *Nationalencyklopedin*, vol. 2 (Bokförlaget Bra Böcker AB, Höganäs, 1990).

14. S. Svanberg, *Atomic and Molecular Spectroscopy*, 2nd ed. (Springer-Verlag, Berlin, 1992).

15. P. R. Carey, *Biochemical Applications of Raman and Resonance Raman Spectroscopies* (Academic Press, New York, 1982).

16. A. Smekal, "Zur Quantentheorie der Dispersion", *Die Naturwissenschaften*, **11**, 873–875 (1923).

17. C. V. Raman and K. S. Krishnan, "A New Type of Secondary Radiation", *Nature*, **121**, 501–502 (1928).

18. C. V. Raman, "A Change of Wave-length in Light Scattering", *Nature*, **121**, 619 (1928).

19. C. V. Raman and K. S. Krishnan, "The Optical Analogue of the Compton Effect", *Nature*, **121**, 711 (1928).

20. G. Landsberg and L. Mandelstam, "Eine neue Erscheinung bei der Lichtzerstreuung in Krystallen", *Die Naturwissenschaften*, **16**, 557–558 (1928).

21. D. A. Long, *Raman Spectroscopy* (McGraw-Hill, New York, 1977).

22. J. Twardowski and P. Anzenbacher, *Raman and IR Spectroscopy in Biology and Biochemistry* (Ellis Horwood, New York, 1994).

23. P. Lorrain, D. P. Corson and F. Lorrain, *Electromagnetic Fields and Waves*, 3rd ed., p. 699 (W. H. Freeman and Company, New York, 1988).

24. D. J. Gardiner and P. R. Graves (eds.), *Practical Raman Spectroscopy* (Springer-Verlag, Berlin, 1989).

25. N. B. Colthup, L. H. Daly and S. E. Wiberley, *Introduction to Infrared and Raman Spectroscopy*, 3rd ed. (Academic Press, San Diego, 1990).

26. F. R. Dollish, W. G. Fateley and F. F. Bentley, *Characteristic Raman Frequencies of Organic Compounds* (John Wiley & Sons, New York, 1974).

27. B. Schrader, *Raman/Infrared Atlas of Organic Compounds*, 2nd ed. (VCH Verlagsgesellschaft, Weinheim, 1989).

28. J. G. Grasselli and B. J. Bulkin (eds.), *Analytical Raman Spectroscopy* (John Wiley & Sons, New York, 1991).

29. J. Funfschilling and D. F. Williams, "CW Laser Wavelength Modulation in Raman and Site Selection Fluorescence Spectroscopy", *Applied Spectroscopy*, **30**, 443–446 (1976).

30. A. P. Shreve, N. J. Cherepy and R. A. Mathies, "Effective Rejection of Fluorescence Interference in Raman Spectroscopy Using a Shifted Excitation Difference Technique", *Applied Spectroscopy*, **46**, 707–711 (1992).

31. T. Tahara and H. Hamaguchi, "Picosecond Raman Spectroscopy Using a Streak Camera", *Applied Spectroscopy*, **47**, 391–398 (1993).

32. S. M. Angel, M. K. DeArmond, K. W. Hanck and D. W. Wertz, "Computer-Controlled Instrument for the Recovery of a Resonance Raman Spectrum in the Presence of Strong Luminescence", *Analytical Chemistry*, **56**, 3000–3001 (1984).

33. P. A. Mosier-Boss, S. H. Lieberman and R. Newbery, "Fluorescence Rejection in Raman Spectroscopy by Shifted-Spectra, Edge Detection, and FFT Filtering Techniques", *Applied Spectroscopy*, **49**, 630–638 (1995).

34. G. Turrell and J. Corset (eds.), *Raman Microscopy* (Academic Press, London, 1996).

35. G. J. Rosasco, E. S. Etz and W. A Cassatt, "The Analysis of Discrete Fine Particles by Raman Spectroscopy", *Applied Spectroscopy*, **29**, 396–404 (1975).

36. J. A. Centeno, K. G. Ishak, F. G. Mullick, W. A. Gahl and T. J. O'Leary, "Infrared Microspectroscopy and Laser Raman Microprobe in the Diagnosis of Cystinosis", *Applied Spectroscopy*, **48**, 569–572 (1994).

37. H. Ishida, R. Kamoto, S. Uchida, A. Ishitani, Y. Ozaki, K. Iriyama, E. Tsukie, K. Shibata, F. Ishihara and H. Kameda, "Raman Microprobe and Fourier Transform-Infrared Microsampling Studies of the Microstructure of Gallstones", *Applied Spectroscopy*, **41**, 407–412 (1987).

38. L. Markwort, B. Kip, E. Da Silva and B. Roussel, "Raman Imaging of Heterogeneous Polymers: A Comparison of Global versus Point Illumination", *Applied Spectroscopy*, **49**, 1411–1430 (1995).

39. N. M. Sijtsema, J. J. Duindam, G. J. Puppels, C. Otto and J. Greve, "Imaging with Extrinsic Raman Labels", *Applied Spectroscopy*, **50**, 545–551 (1996).

40. R. Tabaksblat, R. J. Meier and B. J. Kip, "Confocal Raman Microspectroscopy: Theory and Application to Thin Polymer Samples", *Applied Spectroscopy*, **46**, 60–68 (1992).

41. C. J. H. Brenan and I. W. Hunter, "Confocal Image Properties of a Confocal Scanning Laser Visible Light FT-Raman Microscope", *Applied Spectroscopy*, **49**, 971–976 (1995).

42. C.-H. Liu, B. B. Das, W. L. Sha Glassman, G. C. Tang, K. M. Yoo, H. R. Zhu, D. L. Akins, S. S. Lubicz, J. Cleary, R. Prudente, E. Celmer, A. Caron and R. R. Alfano, "Raman, Fluorescence, and Time-Resolved Light Scattering as Optical Diagnostic Techniques to Separate Diseased and Normal Biomedical Media", *Journal of Photochemistry and Photobiology B: Biology*, **16**, 187–209 (1992).

43. Y. Ozaki, A. Mizuno, H. Sato, K. Kawauchi and S. Muraishi, "Biomedical Application of Near-Infrared Fourier Transform Raman Spectroscopy. Part I: The 1064-nm Excited Raman Spectra of Blood and Met Hemoglobin", *Applied Spectroscopy*, **46**, 533–536 (1992).

44. A. Mizuno, H. Kitajima, K. Kawauchi, S. Muraishi and Y. Ozaki, "Near-Infrared Fourier Transform Raman Spectroscopic Study of Human Brain Tissues and Tumours", *Journal of Raman Spectroscopy*, **25**, 25–29 (1994).

45. A. Mahadevan-Jansen and R. Richards-Kortum, "Raman Spectroscopy for the Detection of Cancers and Precancers", *Journal of Biomedical Optics*, **1**, 31–70 (1996).

46. *Power Specifications of Coherent Innova 300 Series Ion Lasers*, Coherent.

47. R. Faiman, "Raman Spectroscopic Studies of Different Forms of Cholesterol and Its Derivatives in the Crystalline State", *Chemistry and Physics of Lipids*, **18**, 84–104 (1977).

48. M. G. Shim and B. C. Wilson, "The Effects of *Ex Vivo* Handling Procedures on the Near-Infrared Raman Spectra of Normal Mammalian Tissues", *Photochemistry and Photobiology*, **63**, 662–671 (1996).

49. D. A. Carter, W. R. Thompson, C. E. Taylor and J. E. Pemberton, "Frequency/Wavelength Calibration of Multipurpose Multichannel Raman Spectrometers. Part II: Calibration Fit Considerations and Calibration Standards", *Applied Spectroscopy*, **49**, 1561–1576 (1995).

50. S. T. Wollman and P. W. Bohn, "Evaluation of Polynomial Fitting Functions for Use with CCD Arrays in Raman Spectroscopy", *Applied Spectroscopy*, **47**, 125–126 (1993).

51. H. Hamaguchi, "Calibrating Multichannel Raman Spectrometers", *Applied Spectroscopy Reviews*, **24**, 137–174 (1988).